Biochemical and Biophysical Research Communications 391 (2010) 542–546

Contents lists available at ScienceDirect

Biochemical and Biophysical Research Communications

journal homepage: www.elsevier.com/locate/ybbrc

Roles of POLD4, smallest subunit of DNA polymerase δ, in nuclear structures and genomic stability of human cells

Qin Miao Huang [a], Tomohiro Akashi [b], Yuji Masuda [c], Kenji Kamiya [c], Takashi Takahashi [a], Motoshi Suzuki [a,*]

[a] Division of Molecular Carcinogenesis, Center for Neurological Diseases and Cancer, Nagoya University Graduate School of Medicine, Nagoya, Japan
[b] Division of Molecular Mycology and Medicine, Center for Neurological Diseases and Cancer, Nagoya University Graduate School of Medicine, Nagoya, Japan
[c] Research Institute for Radiation Biology and Medicine, Hiroshima University, Hiroshima 734-8553, Japan

ARTICLE INFO

Article history:
Received 13 November 2009
Available online 24 November 2009

Keywords:
POLD4
Karyomere
Micronuclei
Cell cycle
DNA replication
DNA damage

ABSTRACT

Mammalian DNA polymerase δ (pol δ) is essential for DNA replication, though the functions of this smallest subunit of POLD4 have been elusive. We investigated pol δ activities *in vitro* and found that it was less active in the absence of POLD4, irrespective of the presence of the accessory protein PCNA. shRNA-mediated reduction of POLD4 resulted in a marked decrease in colony formation activity by Calu6, ACC-LC-319, and PC-10 cells. We also found that POLD4 reduction was associated with an increased population of karyomere-like cells, which may be an indication of DNA replication stress and/or DNA damage. The karyomere-like cells retained an ability to progress through the cell cycle, suggesting that POLD4 reduction induces modest genomic instability, while allowing cells to grow until DNA damage reaches an intolerant level. Our results indicate that POLD4 is required for the *in vitro* pol δ activity, and that it functions in cell proliferation and maintenance of genomic stability of human cells.

Introduction

Eukaryotic DNA polymerase δ (pol δ), a key enzyme that participates in DNA replication and repair, consists of four subunits; POLD1 (catalytic subunit, alternatively called p125), POLD2 (p50), POLD3 (p68), and POLD4 (p12) [1,2]. Among those, POLD4 binds to POLD1, POLD2, and an accessory protein of PCNA, which allows pol δ to exhibit its full activity [1,3].

A previous study showed that the *POLD4* ortholog of *Cdm1* in *Schizosaccharomyces pombe* is a non-essential gene related to cell growth, division, and sensitivity to DNA damaging reagents [4]. *Saccharomyces cerevisiae* does not have a POLD4 counterpart, indicating that POLD4 is dispensable in lower eukaryotic cells. In contrast, siRNA-mediated knockdown of POLD4 caused a significant decrease in the proliferation rate of FGF2-activated mouse-endothelial cells [5]. However, it remains unknown whether POLD4 is required for other types of mammalian cells, such as those related to human cancer, or if it has additional functions in mammalian cells.

In the present study, we analyzed the roles of POLD4 for cell proliferation in human lung cancer cell lines. Our findings indicate that POLD4 is required for maintaining the proper nuclear structures and suggest that the pathological structures reflect elevated DNA damage in chromosomes.

Materials and methods

Antibodies. The antibodies used in this study were anti-POLD4 (POLD4 subunit of pol δ) ascites (2B11, Abnova, Taipei City, Taiwan), anti-lamin B (c-20) (Santa Cruz Biotechnology, Santa Cruz, CA), and anti-γ-tubulin (Sigma–Aldrich, St. Louis, MO).

In vitro pol δ activity. Three- and 4-subunit DNA from pol δ were expressed in *Escherichia coli*, and purified as described previously [6]. pol δ activity was determined in a reaction mixture (25 μl) containing 20 mM HEPES–NaOH (pH 7.5), 50 mM NaCl, 0.2 mg/ml BSA, 1 mM dithiothreitol, 10 mM $MgCl_2$, 1 mM ATP, 0.1 mM each of dGTP, dATP, dCTP, and [α-^{32}P]dTTP, 100 ng poly dA-oligo dT (GE Healthcare, Piscataway, NJ), 86 ng (1.0 pmol as a trimer) of PCNA, and 11–88 ng (46–372 fmol) of pol δ at 30 °C for 10 min. Following incubation, the reactions were terminated with 2 μl of 300 mM EDTA. pol activity was determined with reference to the incorporation of [α-^{32}P]dTMP, as previously described [6].

Colony formation assay. To assess cell proliferation, colony formation assays were performed as previously described [7]. In order to rule out the off-target effect, we designed two independent DNA sequences as follows: MS543F, 5′-GATCCCCagtctctggcatctctatcATTCAAGAGATgatagagatgccagagactTTTTTGGAAA-3; MS544R, 5′-AGCTTTTCCAAAAAagtctctggcatctctatcATCTCTTGAATgatagagatgccagagactGGG-3; MS551F, 5′-GATCCCCgcatctctatcccctatgaATTCAAGAGATtcataggggatagagatgcTTTTTGGAAA-3; and MS552R, 5′-AGCTTTTCCAAAAAgcatctctatccccctatgaATCTCTTGAATtcatagggatagagatgcGGG-3, in which the targeting sequences are indicated in lowercase letters. To construct shRNA vectors, MS543F and MS544R

* Corresponding author. Address: Division of Molecular Carcinogenesis, Center for Neurological Diseases and Cancer, Nagoya University Graduate School of Medicine, Nagoya 466-8550, Japan.
E-mail address: msuzuki@med.nagoya-u.ac.jp (M. Suzuki).

0006-291X/$ - see front matter © 2009 Elsevier Inc. All rights reserved.
doi:10.1016/j.bbrc.2009.11.094

(polD4-5), and MS551F and MS552R (polD4-3-1) were annealed, then inserted between the restriction sites BglII and HindIII in PH1RNAneo [7]. Cells transfected with a vector carrying either polD4-3-1 or polD4-5 were cultured in media containing 1 mg/ml G418 (Invitrogen, Carlsbad, CA 10131-027), which was reduced by 0.2 mg/ml every 2 days until it reached 0.4 mg/ml. When colonies grew to visible seizes, they were fixed by cold methanol for 5 min and stained with 4% Giemsa for 15 min at room temperature.

RNA interference. Transfection was carried out using 50 nmol/L of a small interfering RNA (siRNA) duplex (Sigma–Aldrich) targeting each mRNA, or negative control 1# (Ambion) with Lipofectamine-2000 (Invitrogen). The sequences of si*POLD4* were the same as those of polD4-3-1: *POLD4* (si*D4*) sense, 5′-GCAUCUCUAUCCCCUAUGATT-3′; and antisense, 5′-UCAUAGGGGAUAGAGAUGCTT.

Laser scanning cytometry (LSC). Following an overnight culture, 3×10^5/ml Calu6 cells on coverslips were fixed by cold methanol, washed with PBS, and incubated with 1 mg/ml RNase A in 50 mM Tris–HCl, pH 7.5, at 37 °C for 1 h. Cells were further treated with 50 μg/ml propidium iodide in a mixture containing 180 mM Tris–HCl, pH 7.5, 180 mM NaCl, and 70 mM $MgCl_2$ for 15 min. Nuclei structures and DNA contents were analyzed using a Laser Scanning Cytometer (LSC, Olympus, Tokyo, Japan), with DNA content at the G1 peak regarded as 2N, though Calu6 cells carry a greater amount of DNA chromatin than normal cells.

Cell cycle synchronization. Calu6 cells were synchronized according to the method of Nakagawa et al. [8], with minor modifications. In brief, 24-h treatment with 2 mM thymidine was used to arrest exponentially proliferating cells in the S phase. Cells were then released from arrest by three washes in PBS and grown in fresh medium for 15 h, then 1 μM of aphidicolin was used for the second block for 10 h. After releasing by three washes in PBS, cells were incubated in RPMI1640 containing 5% fetal bovine serum and harvested at various time points.

Immunofluorescence. Following an overnight culture, 3×10^5/ml Calu6 cells on coverslips were transfected with siRNA as described above. After 48 h, they were fixed in 4% paraformaldehyde for 10 min at room temperature, followed by treatment with cold methanol for 2 min. The coverslips were washed three times in PBS, treated with PBS containing 0.25% Triton X-100 on ice for 30 min, and incubated with anti-lamin B or anti-γ-tubulin antibody overnight at 4 °C. The cells were then washed three times in PBS, incubated for 1 h with Alexa 488-conjugated secondary antibody (Molecular Probes, OR, USA), and analyzed using an Olympus BX60 (Olympus).

Results and discussion

DNA synthesis activities of pol δ with or without POLD4 in vitro

In order to analyze POLD4 functions related to intrinsic pol δ activity, 3- and 4-subunit structures of pol δ were expressed and purified. In the absence of POLD4, pol δ was less active than the holoenzyme in a reaction containing poly dA–dT as a template primer (Fig. 1A), with a similar result obtained when the accessory protein of PCNA was omitted from the reaction (Fig. 1B). These results are consistent with those of previous studies [1,3] and indicate that POLD4 is required for pol δ to exhibit its full catalytic activity.

POLD4 required for cell proliferation

A previous genetic study of *S. pombe* demonstrated that the *POLD4* ortholog of *Cdm1* is a non-essential gene for cell growth,

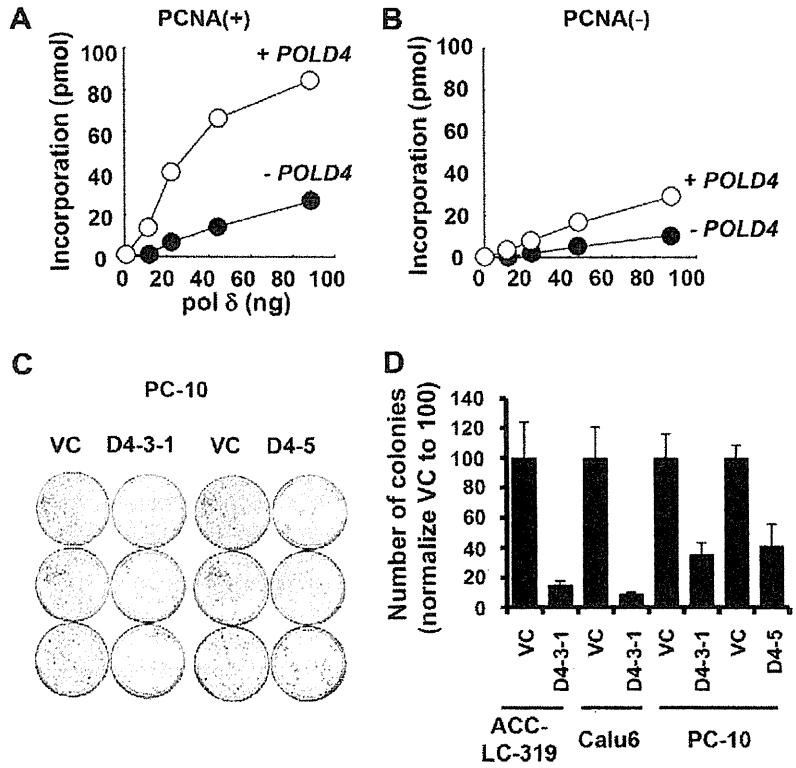

Fig. 1. *In vitro* DNA synthesis activities of pol δ and effect of POLD4 depletion on colony formation activity. (A) pol δ activities were measured and plotted as described in Materials and methods. (B) The same reactions were carried out in the absence of PCNA. (C) PC-10 was used for transfection with plasmids carrying either D4-3-1 or D4-5, and colony formation activity was determined as described in Materials and methods. VC represents vector control. (D) Results of the colony formation assay were plotted in a graph.

division, and sensitivity to DNA damaging reagents [4]. Nevertheless, it is possible that mammalian cells with larger genomic sizes require POLD4 for efficient and accurate DNA replication. We investigated this possibility using shRNA-mediated knockdown of *POLD4*. As shown in Fig. 1C, two independent sequences of shRNA caused reduced activity in a colony formation assay using PC-10, a human non-small cell lung cancer (NSCLC) cell line. Similar results were obtained with different NSCLC cell lines, Calu6 and ACC-LC-319 (Fig. 1D). These findings suggest that human cells require POLD4 for proliferation.

Structure and population of karyomere-like cells following siPOLD4 treatment

Since pol δ is a major DNA replication and repair polymerase, impairment of its activity may cause DNA replication stress, such as accumulation of single-stranded DNA gaps, and inefficient repair of endogenous DNA damage, which ultimately results in cell death. On the other hand, it is also possible that some cells continue to grow following such genetic erosion, which may cause genomic instability. Therefore, we investigated whether POLD4 is also required for suppressing genomic instability in human cells. Initially, we attempted to establish stable clones with low POLD4 expression using shRNA-treated cells. However, clones with adequate levels of POLD4 expression were gradually selected, leading to recovery to the original level over time (data not shown). Therefore, in the following experiments, we used siRNA to transiently reduce POLD4 expression (Fig. 2A, left).

Calu6 cells treated with si*POLD4* formed multiple or lobed nuclei, at a 5.3-fold greater frequency than in the control experiment (Fig. 2B and C). Similar structures were also observed when A549 cells were treated with si*POLD4* (data not shown). Staining with

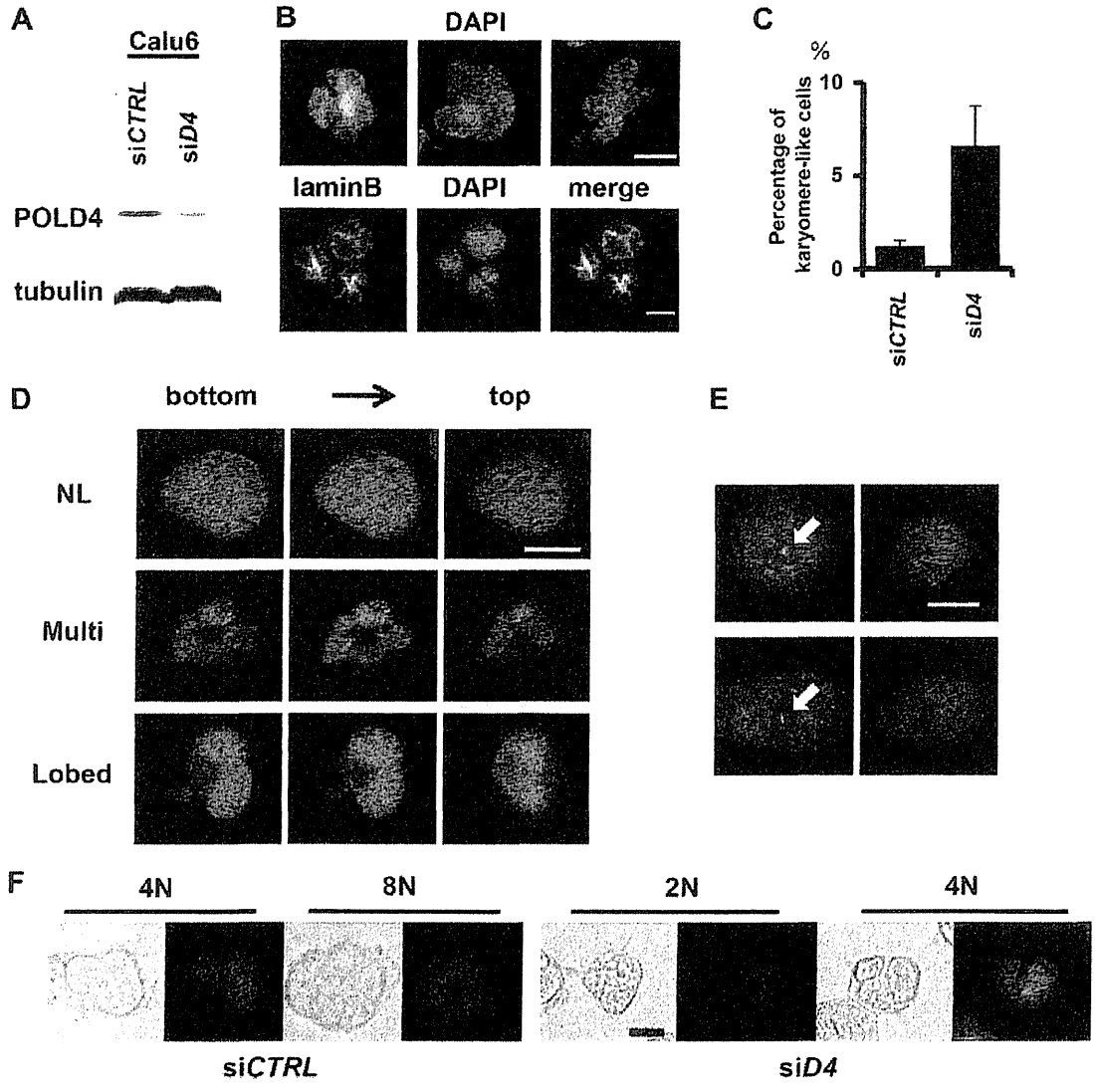

Fig. 2. Structures and population of karyomere-like cells upon si*POLD4* treatment. (A) Western blot analysis of POLD4 and α-tubulin in protein extracts from si*POLD4*- or si*CTRL*-treated Calu6 cells. (B) Upper panels: Calu6 cells were treated with si*POLD4* for 48 h and stained with DAPI. Sample karyomere-like nuclei are shown. Lower panels: Calu6 cells were treated with si*POLD4* for 48 h, then visualized with anti-lamin B antibody or DAPI. (C) Calu6 cells were treated with si*POLD4* or si*CTRL*, then the frequencies of karyomere-like structures in 1000 cells were counted and plotted. In this experiment, cells with three or more nuclear lobes, or three or more nuclei were regarded as karyomere-like cells. Averages of three independent results are shown with SD. (D) si*POLD4*-treated cells were stained by DAPI, then three sequential photographs were taken every 4 μm from the bottom. Upper, middle, and lower panels show images of normal, multiple, and lobed nuclear structures, respectively. (E) After being treated with si*POLD4*, cells were visualized with anti-γ-tubulin (left) or DAPI (right). Upper and lower panels show representative pictures of normal and karyomere-like nuclei, respectively. Centrosomes are indicated by arrows. (F) LSC analysis. Phase-contrast and propidium iodide-stained images of karyomere-like cells among 4N and 8N (si*CTRL*), or 2N and 4N (si*POLD4*) cells. Bar indicates 10 μm.

the anti-lamin B antibody outlined the edges of the DAPI structures and showed that the nuclear envelope was formed around chromatin (Fig. 2B, lower). Sequential acquisition of images from the bottom of the cells further illustrated the abnormal structures of single cells, including a flat profile and multiple nuclei (Fig. 2D, middle panels), or a single nucleus associated with multiple lobes (Fig. 2D, lower panels). For both types of abnormal structures, the nuclear sizes were approximately that of a normally shaped nucleus (Fig. 2D, upper panels).

The multiple nuclei seen with these structures were reminiscent of 'micronuclei' that indicated the presence of DNA damage and DNA replication stress in previous studies [9–11], while the lobed nuclei closely resembled 'karyomere' nuclei observed in zebrafish blastomeres [12] and early *Xenopus laevis* development [13]. In that latter study and other studies referenced therein, it was suggested that karyomere formation is a physiological mitotic process that may share similar mechanisms with pathological micronuclei formation; with both multiple and lobed nuclei, isolated chromosomes might

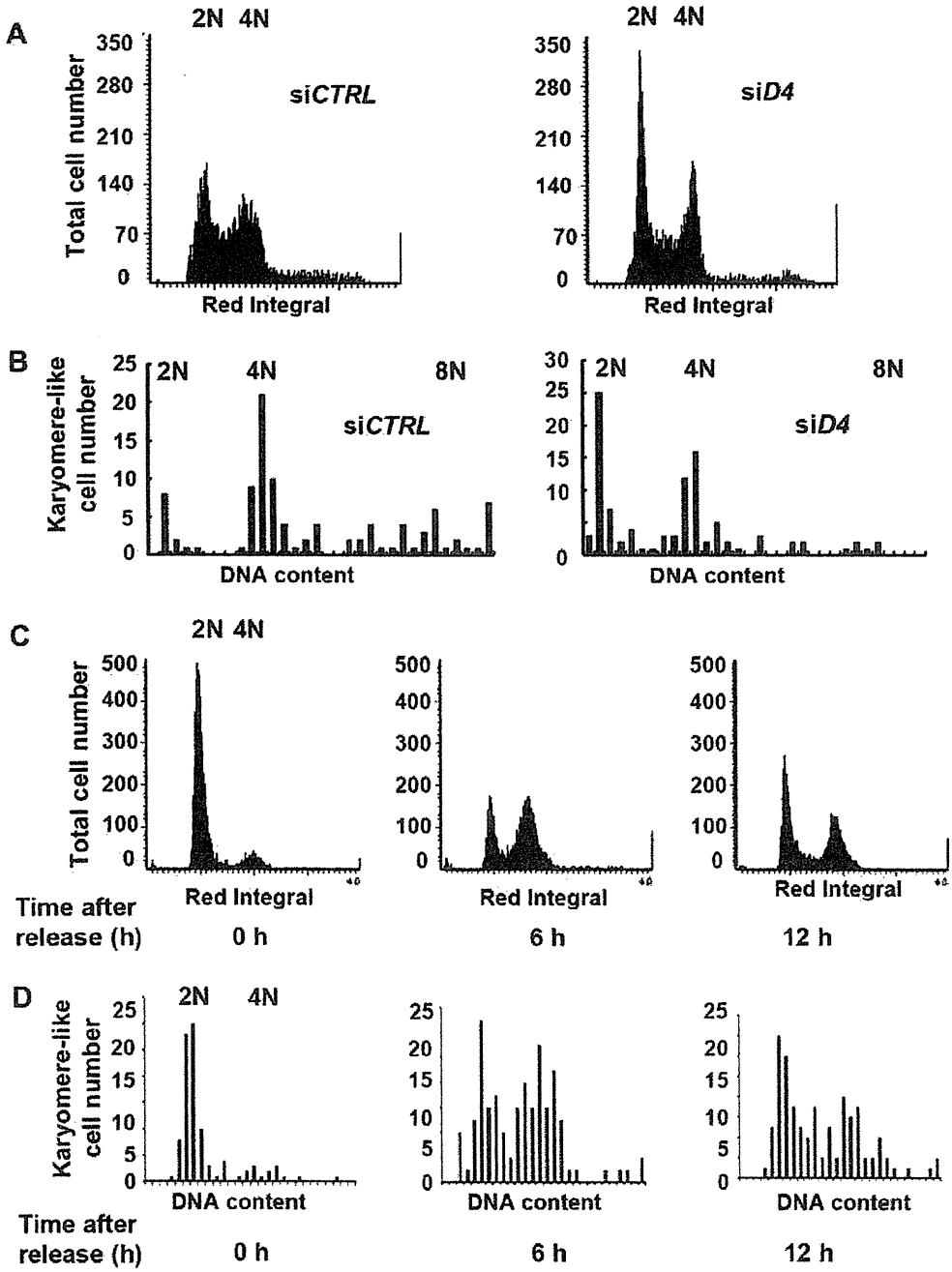

Fig. 3. Cell cycle dynamics of karyomere-like cells. (A) Calu6 cells were treated with si*CTRL* (left) or si*POLD4* (right), then their DNA contents were subjected to LSC analysis. The G1 population found among the majority of cells was regarded as 2N. (B) In the same experiment, DNA contents of 100 karyomere-like cells were determined. Cell numbers in each DNA content range were plotted with histograms. (C) Calu6 cells were treated with si*POLD4*, then synchronized at the G1/S boundary and released for cell cycle progression. At 0, 6, or 12 h after release, DNA contents were subjected to LSC. (D) In the same experiment, the DNA contents of 100 karyomere-like cells were measured. Cell numbers in each DNA content range were plotted with histograms.

be surrounded by a nuclear envelope after chromosome segregation occurs. Therefore, those two types of abnormal structures are referred to as karyomere-like nuclei hereafter.

In addition to DNA damage, formation of karyomere-like nuclei may also occur as a consequence of dysfunctions of the mitotic apparatus [13,14]. Moreover, a previous study found that the anti-POLD4 antibody bound the surface of mitotic chromosomes, which suggests specific functions of POLD4 during mitosis [5]. To investigate this, we analyzed the centrosome structures in si *POLD4*-treated cells, as it has been reported that disturbed chromosomal migration occurred with abnormal replication or localization of centrosomes [15,16]. Our present results showed that si *POLD4*-treated cells were associated with normal centrosome structures, which had one or two centrosomes located at a single site (Fig. 2E). We also quantified the lagging-chromosome frequencies, and found that they were very similar between si*POLD4*- and si*CTRL*-treated mitotic cells (data not shown). Although the results of this limited experiment were contrary to our speculation that POLD4 has some mitotic functions, we intend to conduct more detailed examinations in the future.

Cell cycle dynamics of karyomere-like cells

In the following experiments, we studied the cell cycle dynamics of karyomere-like cells. After si*POLD4* treatment, we observed checkpoint activation (data not shown, detailed mechanisms discussed elsewhere), and accumulations of G1- and G2-populations (Fig. 3A). In si*CTRL*-treated cells, most of the karyomere-like populations were found among the minor aneuploid populations (Figs. 3B and 2F, left panels). In contrast, karyomere-like cells in si *POLD4*-treated cells were found to have normal ploidy as seen with 2N–4N cells (Fig. 3B, 2F, right panels).

In order to determine if karyomere-like cells remained alive and had an ability to progress through the cell cycle, we synchronized cells at the G1–S boundary, then released them and observed the cell cycle progression, as well as the associated nuclear shapes (Fig. 3C–E). Interestingly, karyomere-like cells progressed through the cell cycle and returned to G1 at 12 h after release. In support of these results, most karyomere-like cells were negative in TUNEL staining findings (data not shown). Therefore, these structures may not reflect the pro-apoptotic phenotype. Our results suggest that most karyomere-like cells are able to proliferate until they became arrested at the G1 or G2 phase, when DNA damage reaches an intolerant level.

In conclusion, our results showed that POLD4 supports cellular proliferation and suppresses karyomere-like nuclei formation in human cells, which might occur as a consequence of impairment of the DNA replication and repair activities of pol δ. A future study to identify the direct link between POLD4 and mitotic functions may reveal the underlying mechanisms to maintain genomic stability in human cells.

Acknowledgments

We thank Keiko Ueda and Makiko Terada for their initial involvement in this project. We are also grateful for Dr. Takeshi Senga of our university for the critical reading of the manuscript. This work was supported in part by a Grant-in-Aid for Scientific Research on Innovative Areas, a Grant-in-Aid for Scientific Research on Priority Areas from the Ministry of Education, Culture, Sports, Science, and Technology of Japan, and a Grant-in-Aid for Scientific Research from the Japan Society for the Promotion of Science.

References

[1] V.N. Podust, L.S. Chang, R. Ott, G.L. Dianov, E. Fanning, Reconstitution of human DNA polymerase delta using recombinant baculoviruses: the p12 subunit potentiates DNA polymerizing activity of the four-subunit enzyme, J. Biol. Chem. 277 (2002) 3894–3901.
[2] L. Liu, J. Mo, E.M. Rodriguez-Belmonte, M.Y. Lee, Identification of a fourth subunit of mammalian DNA polymerase delta, J. Biol. Chem. 275 (2000) 18739–18744.
[3] H. Li, B. Xie, Y. Zhou, A. Rahmeh, S. Trusa, S. Zhang, Y. Gao, E.Y. Lee, M.Y. Lee, Functional roles of p12, the fourth subunit of human DNA polymerase delta, J. Biol. Chem. 281 (2006) 14748–14755.
[4] N. Reynolds, A. Watt, P.A. Fantes, S.A. MacNeill, Cdm1, the smallest subunit of DNA polymerase d in the fission yeast *Schizosaccharomyces pombe*, is non-essential for growth and division, Curr. Genet. 34 (1998) 250–258.
[5] P. Dell'Era, S. Nicoli, G. Peri, M. Nieddu, M.G. Ennas, M. Presta, FGF2-induced upregulation of DNA polymerase-delta p12 subunit in endothelial cells, Oncogene 24 (2005) 1117–1121.
[6] Y. Masuda, M. Suzuki, J. Piao, Y. Gu, T. Tsurimoto, K. Kamiya, Dynamics of human replication factors in the elongation phase of DNA replication, Nucleic Acids Res. 35 (2007) 6904–6916.
[7] H. Tanaka, K. Yanagisawa, K. Shinjo, A. Taguchi, K. Maeno, S. Tomida, Y. Shimada, H. Osada, T. Kosaka, H. Matsubara, T. Mitsudomi, Y. Sekido, M. Tanimoto, Y. Yatabe, T. Takahashi, Lineage-specific dependency of lung adenocarcinomas on the lung development regulator TTF-1, Cancer Res. 67 (2007) 6007–6011.
[8] T. Nakagawa, Y. Hayashita, K. Maeno, A. Masuda, N. Sugito, H. Osada, K. Yanagisawa, H. Ebi, K. Shimokata, T. Takahashi, Identification of decatenation G2 checkpoint impairment independently of DNA damage G2 checkpoint in human lung cancer cell lines, Cancer Res. 64 (2004) 4826–4832.
[9] N. Holland, C. Bolognesi, M. Kirsch-Volders, S. Bonassi, E. Zeiger, S. Knasmueller, M. Fenech, The micronucleus assay in human buccal cells as a tool for biomonitoring DNA damage: the HUMN project perspective on current status and knowledge gaps, Mutat. Res. 659 (2008) 93–108.
[10] J.B. Bae, S.S. Mukhopadhyay, L. Liu, N. Zhang, J. Tan, S. Akhter, X. Liu, X. Shen, L. Li, R.J. Legerski, Snm1B/Apollo mediates replication fork collapse and S phase checkpoint activation in response to DNA interstrand cross-links, Oncogene 27 (2008) 5045–5056.
[11] D.J. Kirkland, L. Henderson, D. Marzin, L. Muller, J.M. Parry, G. Speit, D.J. Tweats, G.M. Williams, Testing strategies in mutagenicity and genetic toxicology: an appraisal of the guidelines of the European Scientific Committee for Cosmetics and Non-Food Products for the evaluation of hair dyes, Mutat. Res. 588 (2005) 88–105.
[12] V.K. Schoft, A.J. Beauvais, C. Lang, A. Gajewski, K. Prufert, C. Winkler, M.A. Akimenko, M. Paulin-Levasseur, G. Krohne, The lamina-associated polypeptide 2 (LAP2) isoforms beta, gamma and omega of zebrafish: developmental expression and behavior during the cell cycle, J. Cell Sci. 116 (2003) 2505–2517.
[13] J.M. Lemaitre, G. Geraud, M. Mechali, Dynamics of the genome during early *Xenopus laevis* development: karyomeres as independent units of replication, J. Cell Biol. 142 (1998) 1159–1166.
[14] M. Ohsugi, K. Adachi, R. Horai, S. Kakuta, K. Sudo, H. Kotaki, N. Tokai-Nishizumi, H. Sagara, Y. Iwakura, T. Yamamoto, Kid-mediated chromosome compaction ensures proper nuclear envelope formation, Cell 132 (2008) 771–782.
[15] D. Eriksson, P.O. Lofroth, L. Johansson, K.A. Riklund, T. Stigbrand, Cell cycle disturbances and mitotic catastrophes in HeLa Hep2 cells following 2.5 to 10 Gy of ionizing radiation, Clin. Cancer Res. 13 (2007) 5501s–5508s.
[16] H. Dodson, E. Bourke, L.J. Jeffers, P. Vagnarelli, E. Sonoda, S. Takeda, W.C. Earnshaw, A. Merdes, C. Morrison, Centrosome amplification induced by DNA damage occurs during a prolonged G2 phase and involves ATM, EMBO J. 23 (2004) 3864–3873.

Published online 17 July 2010

Nucleic Acids Research, 2010, Vol. 38, No. 21 7579–7586
doi:10.1093/nar/gkq630

Single-stranded DNA catenation mediated by human EVL and a type I topoisomerase

Motoki Takaku[1], Daisuke Takahashi[1], Shinichi Machida[1], Hiroyuki Ueno[1], Noriko Hosoya[2], Shukuko Ikawa[3], Kiyoshi Miyagawa[2], Takehiko Shibata[3] and Hitoshi Kurumizaka[1,*]

[1]Laboratory of Structural Biology, Graduate School of Advanced Science and Engineering, Waseda University, 2-2 Wakamatsu-cho, Shinjuku-ku, Tokyo 162-8480, [2]Laboratory of Molecular Radiology, Center of Disease Biology and Integrative Medicine, Graduate School of Medicine, The University of Tokyo, 7-3-1 Hongo, Bunkyo-ku, Tokyo 113-0033 and [3]RIKEN Advanced Science Institute, 2-1 Hirosawa, Wako-shi, Saitama 351-0198, Japan

Received April 5, 2010; Accepted June 30, 2010

ABSTRACT

The human Ena/Vasp-like (EVL) protein is considered to be a bifunctional protein, involved in both actin remodeling and homologous recombination. In the present study, we found that human EVL forms heat-stable multimers of circular single-stranded DNA (ssDNA) molecules in the presence of a type I topoisomerase *in vitro*. An electron microscopic analysis revealed that the heat-stable ssDNA multimers formed by EVL and topoisomerase were ssDNA catemers. The ssDNA catenation did not occur when either EVL or topoisomerase was omitted from the reaction mixture. A deletion analysis revealed that the ssDNA catenation completely depended on the annealing activity of EVL. Human EVL was captured from a human cell extract by TOPO IIIα-conjugated beads, and the interaction between EVL and TOPO IIIα was confirmed by a surface plasmon resonance analysis. Purified TOPO IIIα catalyzed the ssDNA catenation with EVL as efficiently as the *Escherichia coli* topoisomerase I. Since the ssDNA cutting and rejoining reactions, which are the sub-steps of ssDNA catenation, may be an essential process in homologous recombination, EVL and TOPO IIIα may function in the processing of DNA intermediates formed during homologous recombination.

INTRODUCTION

Human Ena/Vasp-like (EVL) is a member of the ENA/VASP family, which is involved in actin-remodeling processes (1). We previously reported (2) that EVL may also function in homologous recombination, because it directly binds to RAD51 and RAD51B, which are essential proteins for meiotic homologous recombination and mitotic recombinational repair of DNA double-strand breaks (3–6). Biochemical studies revealed that EVL forms tetramer-based multimers, and actually stimulates the RAD51-mediated recombinase reactions, such as homologous pairing and strand exchange, *in vitro* (2,7). In addition to the RAD51-stimulating activity, EVL also possesses ssDNA annealing activity (2), which is considered to be important for the homologous-recombination processes. Therefore, EVL may have dual functions in cytoplasmic actin remodeling and nuclear homologous recombination.

Topoisomerases promote DNA strand cutting and rejoining, and are known to be important in homologous recombination. *Escherichia coli* RecA, a bacterial homolog of RAD51, forms homologous joint molecules between circular ssDNA and closed circular dsDNA by its recombinase activity (8). *Escherichia coli* topoisomerase I (Topo I) reportedly converts the homologous joint molecules formed by RecA into hemicatemers (8). *Escherichia coli* topoisomerase III efficiently catenates closed circular dsDNAs in the presence of RecQ helicase (9,10), which is suggested to function in homologous recombination. In humans, TOPO IIIα forms a complex with BLM and BLAP75 (11,12), and the complex is reportedly involved in the dissolution of the Holliday junction (13–18), which is a DNA intermediate formed in the late stage of homologous recombination. These facts suggest that the DNA cutting and rejoining activities of topoisomerases play important roles in homologous recombination.

In the present study, we unexpectedly found that EVL, with either *E. coli* Topo I or human TOPO IIIα, catalyzed

*To whom correspondence should be addressed. Tel: +81 3 5369 7315; Fax: +81 3 5367 2820; Email: kurumizaka@waseda.jp

ssDNA catenation. The omission of either EVL or topoisomerase quenched the ssDNA-catenating reaction, indicating that both proteins are essential for this reaction. A deletion analysis revealed that the EVL C-terminal domain, which possesses the annealing activity, is responsible for the ssDNA catenation. We also found that EVL physically interacted with human TOPO IIIα in a human cell extract and *in vitro*. These new findings suggest that EVL may function with a type I topoisomerase, such as TOPO IIIα, by catalyzing ssDNA cutting and re-joining reactions in the conversion of DNA intermediates during homologous recombination.

MATERIALS AND METHODS

Protein preparation

Human EVL, EVL(1–221) and EVL(222–418) were prepared by the methods described earlier (2,7). In these methods, human EVL, EVL(1–221) and EVL(222–418) were expressed as His_6-tagged proteins, and the His_6 tag was removed by a thrombin treatment during the purification procedure. Human RPA was produced in *E. coli* cells and was prepared according to the published protocol (19).

The DNA fragment encoding human TOPO IIIα was isolated from a human cDNA pool (purchased from Clontech Laboratories, Mountain View, CA, USA) by the polymerase chain reaction. The TOPO IIIα DNA fragment was cloned in the *Nde*I site of the pET15b vector (Novagen, Darmstadt, Germany). In this construct, the His_6 tag sequence was fused to the N terminus of the protein. Human TOPO IIIα was produced in the *E. coli* BL21(DE3) codon plus-RP strain (Stratagene, La Jolla, CA, USA) and was purified by the following procedure. The cells producing His_6-tagged TOPO IIIα were resuspended in a 50 mM Tris–HCl buffer (pH 7.5), containing 1M NaCl, 5 mM 2-mercaptoethanol and 10% glycerol, and were disrupted by sonication. The cell debris was removed by centrifugation for 20 min at 30 000*g*, and the lysate was mixed gently by the batch method with Ni-NTA agarose beads (3 ml, Qiagen, Hilden, Germany) at 4°C for 1 h. The His_6-tagged TOPO IIIα-bound beads were washed with 40 ml of 20 mM potassium phosphate buffer (pH 7.4), containing 500 mM NaCl, 5 mM 2-mercaptoethanol, 40 mM imidazole and 10% glycerol, and then were washed again with 40 ml of 20 mM potassium phosphate buffer (pH 7.4), containing 500 mM NaCl, 5 mM 2-mercaptoethanol, 30 mM imidazole and 10% glycerol. The beads were then packed into an Econo-column (Bio-Rad Laboratories, Hercules, CA, USA) and were washed with 90 ml of 20 mM potassium phosphate buffer (pH 7.4), containing 500 mM NaCl, 5 mM 2-mercaptoethanol, 30 mM imidazole and 10% glycerol. His_6-tagged TOPO IIIα was eluted with a linear gradient of 30–300 mM imidazole (13-column volumes), in 20 mM potassium phosphate (pH 7.4), 100 mM NaCl, 5 mM 2-mercaptoethanol and 10% glycerol. Peak fractions containing His_6-tagged TOPO IIIα were diluted 5-fold with a 20 mM potassium phosphate buffer (pH 7.4), containing 5 mM 2-mercaptoethanol and 10% glycerol and were mixed gently by the batch method with Hydroxyapatite resin (5 ml, Bio-Rad Laboratories) at 4°C for 1 h. The unbound fraction was then dialyzed against a 20 mM potassium phosphate buffer (pH 7.4), containing 100 mM NaCl, 5 mM 2-mercaptoethanol and 10% glycerol. After the dialysis, the sample was loaded on an SP Sepharose column (1 ml, GE Healthcare Biosciences, Uppsala, Sweden), which was equilibrated with 20 ml of 20 mM potassium phosphate buffer (pH 7.4), containing 100 mM NaCl, 5 mM 2-mercaptoethanol and 10% glycerol. The resin was washed with 20 ml of 20 mM potassium phosphate buffer (pH 7.4), containing 225 mM NaCl, 5 mM 2-mercaptoethanol and 10% glycerol, and the His_6-tagged TOPO IIIα was then eluted with a linear gradient of 225–600 mM NaCl (24-column volumes). The purified His_6-tagged TOPO IIIα was dialyzed against 20 mM HEPES–NaOH buffer (pH 7.5), containing 100 mM NaCl, 5 mM 2-mercaptoethanol and 20% glycerol, and was stored at −80°C. The concentration of the purified His_6-tagged TOPO IIIα was determined by the Bradford method (20), using bovine serum albumin as the standard.

Assays for DNA binding

The ϕX174 circular ssDNA (20 μM) was mixed with EVL in 10 μl of a standard reaction solution, containing 36 mM HEPES–NaOH (pH 7.5), 1 mM dithiothreitol, 4 mM 2-mercaptoethanol, 80 mM NaCl, 1 mM $MgCl_2$, 24% glycerol and 0.1 mg/ml bovine serum albumin. The reaction mixtures were incubated at 37°C for 15 min, and were then analyzed by 0.8% agarose gel electrophoresis in 1× TAE buffer (40 mM Tris–acetate and 1mM EDTA) at 3.3 V/cm for 2 h. The bands were visualized by ethidium bromide staining.

ssDNA-catenating assay

The ϕX174 circular ssDNA (20 μM) was incubated with EVL and Topo I (New England Biolabs, Ipswich, MA, USA), in a reaction buffer containing 24 mM HEPES–NaOH (pH 7.5), 1 mM $MgCl_2$, 1 mM Tris–HCl (pH 7.5), 1.1 mM dithiothreitol, 1 mM 2-mercaptoethanol, 20 mM NaCl, 5 mM KCl, 3.5 mM ammonium sulfate, 0.01 mM EDTA, 11% glycerol and 0.1 mg/ml bovine serum albumin, at 37°C for 1 h. For the experiments with TOPO IIIα, the reactions were conducted in a buffer containing 30 mM HEPES–NaOH (pH 7.5), 1 mM $MgCl_2$, 1 mM dithiothreitol, 2.5 mM 2-mercaptoethanol, 70 mM NaCl, 14% glycerol and 0.1 mg/ml bovine serum albumin. The samples were then deproteinized by a treatment with 0.2% SDS and 1.3 mg/ml proteinase K at 37°C for 15 min. The products were then incubated at 100°C for 5 min and were chilled on ice for 5 min. The products were separated by 1% agarose gel electrophoresis, and the bands were visualized by SYBR Gold (Invitrogen, Carlsbad, CA, USA) staining.

ssDNA-annealing assay

The ssDNA-annealing assay was performed as described earlier (2). Briefly, the ssDNA oligonucleotide 49-mer (0.2 μM) was incubated with the indicated amounts of

EVL or the EVL fragments at 30°C for 5 min, in 9 µl of reaction buffer, containing 28 mM HEPES–NaOH (pH 7.5), 50 mM NaCl, 2 mM 2-mercaptoethanol, 12% glycerol, 0.1 mM $MgCl_2$, 1 mM DTT and 0.1 mg/ml bovine serum albumin. The reactions were initiated by the addition of 0.2 µM antisense ^{32}P-labeled 49-mer oligonucleotide. At the times indicated, the reactions were quenched with an excess of the unlabeled 49-mer oligonucleotide. The DNA substrates and products were deproteinized by a treatment with 0.2% SDS and 1.5 mg/ml proteinase K at 30°C for 10 min. The products were fractionated by 10% PAGE in 0.5× TBE. The gels were dried, exposed to an imaging plate and visualized using an FLA-7000 imaging analyzer (Fujifilm, Tokyo, Japan).

Electron microscopic analysis

The ssDNA catemers formed by EVL and Topo I were extracted by phenol/chloroform and precipitated with ethanol. The ssDNA catemers were then coated with RecA in the absence of ATP and were stained on a copper-plated carbon grid with 2% uranyl acetate. The samples were visualized by tungsten rotary shadowing, and were observed with a JEOL JEM 2000FX electron microscope (JEOL, Akishima, Tokyo, Japan).

Pull-down assays with TOPO IIIα-conjugated beads

Purified human TOPO IIIα was covalently conjugated to Affi-Gel 10 beads (100 µl, Bio-Rad), according to the manufacturer's instructions. To block the remaining active ester sites, ethanolamine (pH 8.0) was added to a final concentration of 100 mM, and the resin was incubated at 4°C overnight. The unbound proteins were removed by washing the Affi-Gel 10-TOPO IIIα beads three times with 500 µl of binding buffer, which contained 20 mM HEPES–NaOH (pH 7.5), 300 mM NaCl, 5 mM 2-mercaptoethanol, 20% glycerol and 0.05% Triton X-100. After washing the resin, the Affi-Gel 10-protein matrices were adjusted to 50% slurries, and were stored at 4°C. The control beads were made by the same method, except that the TOPO IIIα was replaced by the TOPO IIIα storage buffer. For the EVL-binding assay, the TOPO IIIα-beads were incubated with an MCF7 whole-cell extract (1.8 mg of protein), and the beads were washed three times with 200 µl of washing buffer, containing 50 mM Tris–HCl (pH 7.5), 100 mM NaCl, 5 mM EDTA, 0.5% NP-40, 1 mM phenylmethylsulfonyl fluoride and protease inhibitor cocktail (Nacalai Tesque, Kyoto, Japan). The proteins that copelleted with the TOPO IIIα beads were fractionated by 7.5% SDS–PAGE. The EVL protein was detected with the EVL-specific rabbit polyclonal antibodies.

Surface plasmon resonance analysis

The surface plasmon resonance (SPR) signals were measured with a Biacore X100 instrument (GE Healthcare Biosciences, Uppsala, Sweden). Flow cells were maintained at 25°C during the measurement, and the instrument was operated at the mid-flow rate (~30 µl/min). Purified EVL was conjugated to the activated surface of the CM5 sensor chip (GE Healthcare Biosciences, Uppsala, Sweden), using the standard amine coupling conditions recommended by the manufacturer. The level of the conjugated EVL protein was 5600 resonance units. The SPR signals of the flow cell containing a sensor chip without the proteins were subtracted from those of the SPR signals of the flow cell containing the EVL-conjugated sensor chip. The running buffer was 20 mM HEPES–NaOH (pH 7.5), 200 mM NaCl, 2.5% glycerol, 1 mM dithiothreitol and 0.1% Tween-20. For the binding assay, 0.1 µM TOPO IIIα, RPA, Topo I or bovine serum albumin was injected for 2 min.

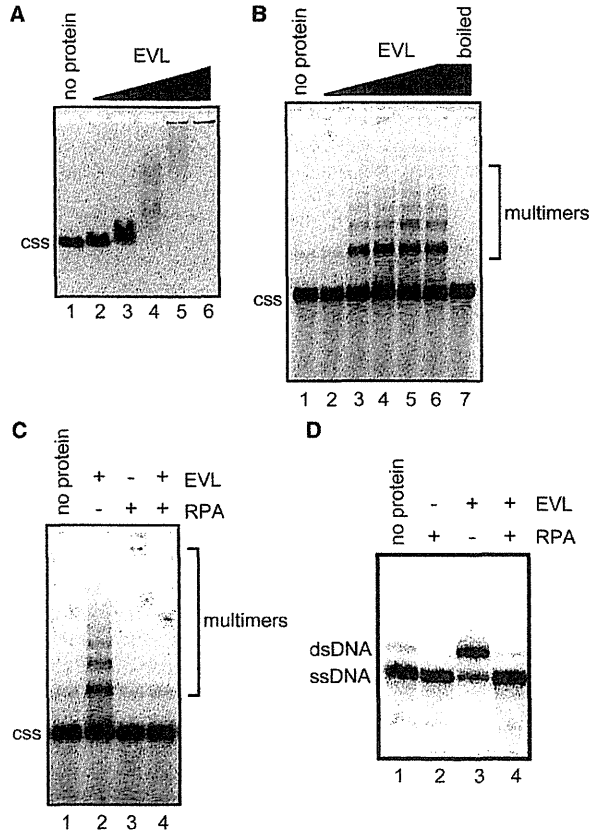

Figure 1. EVL promotes the formation of circular ssDNA multimers. (**A**) The ssDNA-binding assay. ϕX174 ssDNA (20 µM) was incubated with the EVL protein at 37°C for 15 min. The samples were then separated by 0.8% agarose gel electrophoresis in TAE buffer and were visualized by ethidium bromide staining. Lane 1 indicates a negative control experiment without the protein. Lanes 2–6 indicate the experiments with EVL. The concentrations of EVL were 0.1 µM (lane 2), 0.2 µM (lane 3), 0.4 µM (lane 4), 0.8 µM (lane 5) and 1.6 µM (lane 6). The ϕX174 circular ssDNA molecule is indicated by css. (**B**) Multimer formation. ϕX174 circular ssDNA (20 µM) was incubated with EVL. The samples were then separated by 1% agarose gel electrophoresis and were visualized by SYBR Gold staining. The concentrations of EVL were 0.125 µM (lane 2), 0.25 µM (lane 3), 0.5 µM (lane 4), 1 µM (lane 5) and 2 µM (lanes 6 and 7). Lane 7 was incubated at 100°C for 5 min. Lane 1 indicates a negative control experiment without the protein. (**C**) Inhibition of ssDNA multimer formation by RPA. ϕX174 circular ssDNA (20 µM) was incubated with EVL (1 µM) in the presence or absence of RPA (2 µM). (**D**) Inhibition of the EVL-mediated ssDNA annealing by RPA. EVL (1 µM) was first incubated with ssDNA (0.2 µM) in the presence or absence of RPA (80 nM), followed by the addition of a complementary ssDNA. The reactions were conducted at 30°C for 8 min.

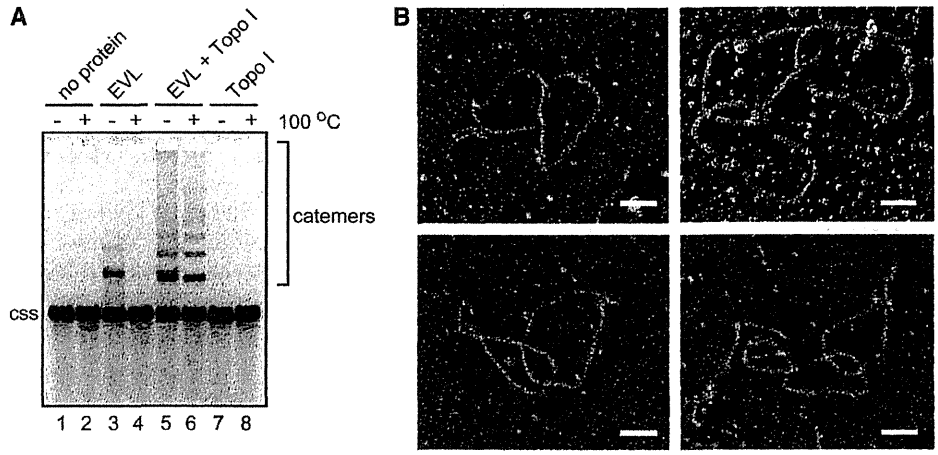

Figure 2. EVL promotes the ssDNA-catenating activity in the presence of Topo I. (**A**) Catemer formation. ϕX174 circular ssDNA (20 μM) was incubated with EVL (1 μM) and Topo I (0.4 nM). Lanes 1 and 2 indicate negative control experiments without the protein. Lanes 3 and 4 indicate the experiments in the presence of EVL. Lanes 5 and 6 indicate the experiments in the presence of EVL and Topo I. Lanes 7 and 8 indicate the experiments in the presence of Topo I. In the experiments shown in lanes 2, 4, 6 and 8, the samples were incubated at 100°C for 5 min before loading on the gel. Lanes 1, 3, 5 and 7 indicate control experiments without the 100°C incubation step. The ϕX174 circular ssDNA molecule is indicated by css. (**B**) Electron microscopic visualization of the ssDNA catemers. Scale bars denote 100 nm.

RESULTS

EVL promotes the formation of circular ssDNA multimers

As described earlier (2), EVL bound to ϕX174 circular ssDNA (5386 bases) and formed large complexes (Figure 1A). We found that ssDNA multimers were formed within this EVL–ssDNA complex, after the EVL protein was removed from the complex by an SDS and proteinase K treatment (Figure 1B). Since we previously reported that EVL promotes the annealing of complementary ssDNAs (2), we suspected that the ssDNA multimers may be annealed products between short, complementary sequences within the ϕX174 circular ssDNA. As anticipated, the ssDNA multimers were dissociated into monomers, when the samples were incubated at 100°C for 5 min (Figure 1B, lane 7). In addition, the formation of the ssDNA multimers by EVL was completely suppressed by an ssDNA-binding protein, RPA (Figure 1C), which significantly inhibited the ssDNA annealing by EVL (Figure 1D). Therefore, we concluded that EVL promotes annealing between short, complementary sequences within the ϕX174 circular ssDNA and forms ssDNA multimers.

EVL promotes ssDNA catenation in the presence of Topo I

The ssDNA multimers formed by EVL may be annealed products, because the multimers were dissociated by heating (Figure 1B). Interestingly, we found that the ssDNA multimers formed by EVL in the presence of a type I topoisomerase, *E. coli* Topo I, were not resolved after incubation at 100°C for 5 min (Figure 2A, lane 6). These heat-stable ssDNA multimers may be ssDNA catemers. To assess whether ssDNA catemers were formed, we visualized the heat-stable ssDNA multimers by electron microscopy. To do so, the ssDNA multimers were purified, and were then coated with RecA to visualize

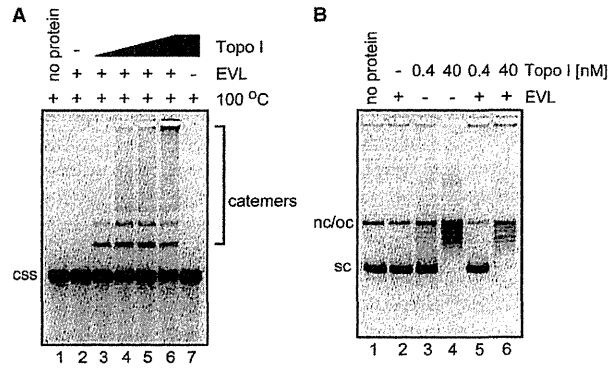

Figure 3. Catalytic function of Topo I in the EVL-mediated ssDNA-catenating reaction. (**A**) ϕX174 circular ssDNA (20 μM) was incubated with Topo I in the presence of EVL. To eliminate the annealed products, the reaction products were treated at 100°C for 5 min before loading on the gel. Lane 1 is a control experiment without the proteins. Lane 2 indicates a negative control experiment without Topo I in the presence of EVL (1 μM). Lanes 3–6 indicate the experiments with various amounts of Topo I in the presence of EVL (1 μM). The concentrations of Topo I are 0.04 nM (lane 3), 0.2 nM (lane 4), 0.4 nM (lane 5) and 0.8 nM (lane 6). Lane 7 indicates a negative control experiment with Topo I (0.8 nM) in the absence of EVL. The ϕX174 circular ssDNA molecule is indicated by css. (**B**) ϕX174 superhelical dsDNA (20 μM) was incubated with EVL (1 μM) and Topo I (0.4 nM or 40 nM). Lane 1 indicates the negative control experiment without the protein. Lanes 2, 5 and 6 indicate the experiments in the presence of EVL (1 μM). Lanes 3 and 5 indicate the experiments in the presence of a low amount of Topo I (0.4 nM). Lanes 4 and 6 indicate the experiments in the presence of a high amount of Topo I (40 nM). ϕX174 superhelical and nicked or open circular dsDNA molecules are indicated by sc and nc/oc, respectively.

the ssDNA. As anticipated, circular ssDNA catemers, containing two or three ssDNA molecules, were observed (Figure 2B). We counted a total of 102 molecules from the DNA samples and found that about 72.5, 18.6, 6.9 and 2% of ssDNA molecules were single circles, two

ssDNA catemers, three ssDNA catemers and four or five ssDNA catemers, respectively. Therefore, we concluded that the heat-stable ssDNA multimers are ssDNA catemers.

The ssDNA-catenating reaction did not occur when either EVL or Topo I was omitted from the reaction mixture (Figure 3A, lanes 2 and 7), indicating that both EVL and Topo I are essential for the ssDNA-catenating reaction. In addition, the formation of EVL-dependent DNA catemers was not detected when circular dsDNA was used as a substrate (Figure 3B). Protein titration experiments revealed that a very small amount of Topo I (0.04 nM) was sufficient to form the ssDNA catemers (Figure 3A, lane 3). This Topo I concentration (0.04 nM) was far below the amount required for inducing a topological change in supercoiled DNA, because 0.4 nM of Topo I is not sufficient to relax supercoiled DNA (Figure 3B, lanes 3 and 5). Therefore, these results suggested that Topo I catalytically functions in the EVL-dependent ssDNA-catenating reaction.

EVL-mediated ssDNA annealing plays an essential role in the ssDNA-catenating reaction

We next tested whether the ssDNA annealing by EVL plays an essential role in the ssDNA-catenating reaction with Topo I. To do so, we prepared two EVL fragments, EVL(1–221) and EVL(222–418), which contained amino acid residues 1–221 and 222–418, respectively (7). As shown in Figure 4A and B, EVL(222–418) promoted annealing to a similar extent as full-length EVL, but EVL(1–221) did not. We then tested whether EVL(1–221) and EVL(222–418) support the ssDNA-catenating reaction. As anticipated, EVL(222–418), which possesses the annealing activity, promoted the ssDNA-catenating reaction, with indistinguishable efficiency from the full-length EVL (Figure 4C, lane 7). In contrast, EVL(1–221) did not promote the ssDNA-catenating reaction (Figure 4C, lane 6). These results indicated that the EVL annealing activity is essential for the ssDNA-catenating reaction with Topo I.

Human TOPO IIIα catalyzes the ssDNA-catenating reaction in the presence of EVL

We then determined whether human topoisomerase can also promote the EVL-dependent ssDNA-catenating reaction. A eukaryotic type I topoisomerase, human TOPO IIIα, reportedly functions in homologous recombination (11–18). Therefore, we purified human TOPO IIIα as a recombinant protein (Figure 5A). The purified TOPO IIIα was chemically conjugated to Affi-Gel 10, and pull-down assays were performed with MCF7 cell extracts. As shown in Figure 5B (lane 3), the endogenous EVL protein in the MCF7 cells was clearly detected in the TOPO IIIα-bound fraction. A SPR analysis also revealed that purified TOPO IIIα efficiently bound to EVL (Figure 5C). We next performed the EVL-dependent ssDNA-catenating assay with TOPO IIIα. As shown in Figure 5D, TOPO IIIα significantly stimulated the ssDNA-catenating reaction in the presence of EVL. Like *E. coli* Topo I (Figure 3A), the ssDNA catemers were

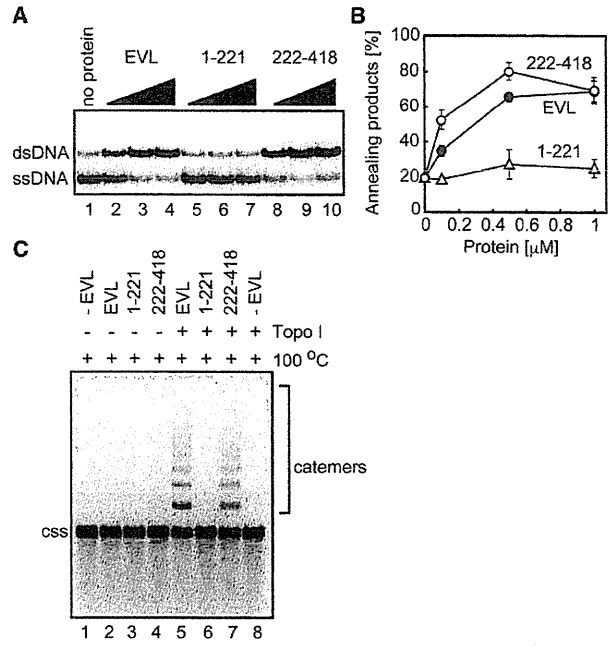

Figure 4. The EVH2 domain is responsible for the ssDNA-annealing activity and the ssDNA-catenation. (**A**) ssDNA annealing activities of EVL(222–418). EVL, EVL(1–221) or EVL(222–418) was first incubated with ssDNA (0.2 μM), followed by the addition of a complementary ssDNA. The reactions were conducted at 30°C for 8 min. Lane 1 indicates a control experiment without protein, and lanes 2–4, lanes 5–7 and lanes 8–10 indicate the experiments with EVL, EVL(1–221) and EVL(222–418), respectively. The EVL, EVL(1–221) and EVL(222–418) concentrations were 0.1 μM (lanes 2, 5 and 8), 0.5 μM (lanes 3, 6 and 9) and 1 μM (lanes 4, 7 and 10). (**B**) Graphical representation of the experiments shown in panel A. The band intensities of the annealed products were quantified, and the average values of three independent experiments are shown with the standard deviation values. Closed circles, open circles and open triangles indicate experiments with EVL, EVL(222–418) and EVL(1–221), respectively. (**C**) Catemer formation with the EVL(222–418) fragment. Lane 1 indicates a control experiment without protein. Lanes 2 and 5 indicate the experiments with EVL. Lanes 3 and 6 indicate the experiments with EVL(1–221). Lanes 4 and 7 indicate the experiments with EVL(222–418). Lanes 5–8 indicate the experiments in the presence of Topo I (0.4 nM). The ϕX174 circular ssDNA molecule is indicated by css.

formed with a very small amount of TOPO IIIα (0.01 nM, Figure 5D, lane 4), suggesting its catalytic function in the reaction. The ssDNA catemers were not formed when either EVL or TOPO IIIα was omitted from the reaction mixture (Figure 5D, lanes 2 and 8). In addition, we found that the ssDNA-catenating reaction mediated by EVL and TOPO IIIα was significantly inhibited by RPA (Figure 6A), which suppresses the EVL-dependent ssDNA annealing (Figure 1C and D). The EVL-TOPO IIIα interaction was still observed in the presence of RPA (Figure 6B). These results suggested that RPA inhibits the ssDNA-catenating reaction by inhibiting the EVL-mediated ssDNA annealing.

Intriguingly, we also found that EVL bound to *E. coli* Topo I, with reduced affinity as compared to human TOPO IIIα *in vitro* (Figure 5C). Although this EVL-Topo I combination does not exist in the natural context, it suggested that EVL binding to the Topo I

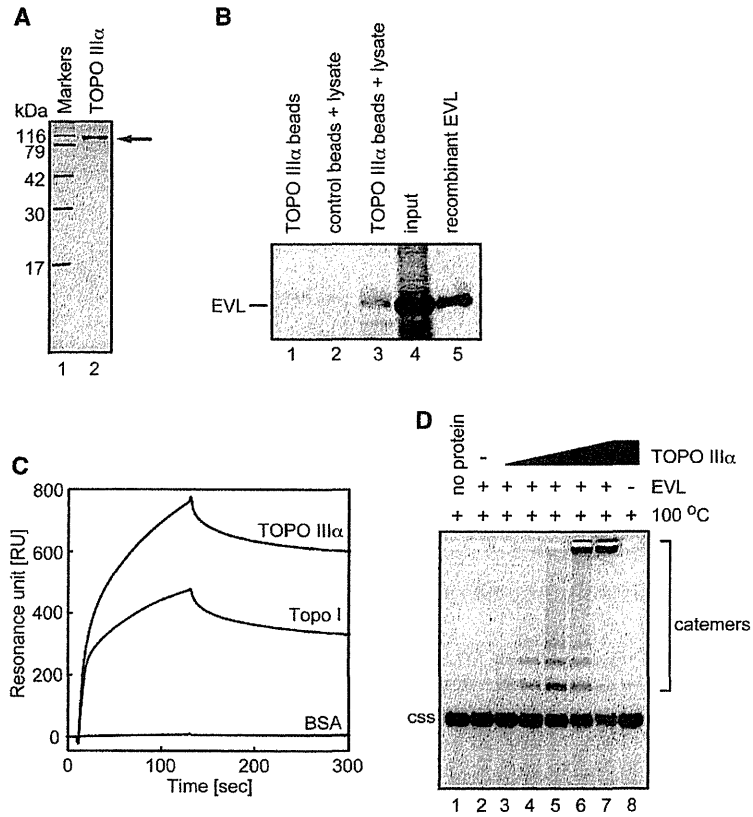

Figure 5. Human TOPO IIIα catalyzes the ssDNA-catenating reaction in the presence of EVL. (**A**) Human TOPO IIIα was purified and analyzed by 15% SDS–PAGE with Coomassie Brilliant Blue staining. (**B**) Pull down assay. Affi-Gel 10 beads chemically conjugated with human TOPO IIIα were incubated with MCF7 whole cell extract. Proteins bound to the TOPO IIIα beads were separated by SDS–PAGE and were analyzed by western blotting. Endogenous EVL was probed with an anti-EVL polyclonal antibody. Lanes 2 and 3 indicate experiments with the control Affi-Gel 10 beads and the TOPO IIIα beads, respectively, in the presence of the MCF7 cell lysate. Lane 1 indicates a control experiment with the TOPO IIIα beads in the absence of the MCF7 cell lysate. The input MCF7 cell lysate (20 μg of protein) and the purified EVL (2 ng) protein were applied in lanes 4 and 5, respectively. (**C**) SPR analysis of the TOPO IIIα-EVL interaction. Sensorgrams for TOPO IIIα, Topo I and bovine serum albumin (BSA) binding to the immobilized EVL protein are presented. (**D**) ϕX174 circular ssDNA (20 μM) was incubated with TOPO IIIα in the presence of EVL. To eliminate the annealed products, the reaction products were treated at 100°C for 5 min before loading on the gel. Lane 1 is a control experiment without the proteins. Lane 2 indicates a negative control experiment without TOPO IIIα in the presence of EVL (1 μM). Lanes 3–7 indicate the experiments with various amounts of TOPO IIIα in the presence of EVL (1 μM). The concentrations of TOPO IIIα are 0.001 nM (lane 3), 0.01 nM (lane 4), 0.05 nM (lane 5), 0.1 nM (lane 6) and 0.5 nM (lane 7). Lane 8 indicates a negative control experiment with TOPO IIIα (0.5 nM) in the absence of EVL. The ϕX174 circular ssDNA molecule is indicated by css.

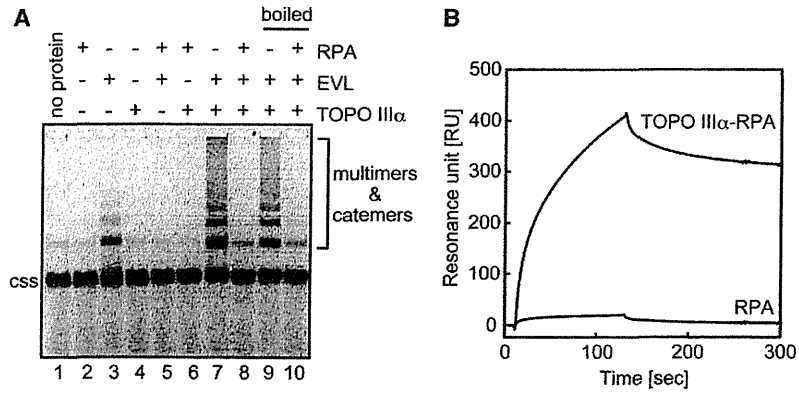

Figure 6. RPA inhibits the ssDNA-catenating reaction mediated by EVL and human TOPO IIIα. (**A**) ϕX174 circular ssDNA (20 μM) was incubated with TOPO IIIα and EVL in the presence or absence of RPA. Lanes 1–8 indicate control experiments without boiling. Lanes 9 and 10 indicate the ssDNA-catenating experiments, in which the reaction products were treated at 100°C for 5 min before loading on the gel. Proteins added to the reactions are indicated on the top of panel A. Protein concentrations were RPA (2 μM), EVL (1 μM) and TOPO IIIα (0.1 nM). (**B**) SPR analysis of the TOPO IIIα–EVL interaction in the presence of RPA. Sensorgrams for TOPO IIIα/RPA and RPA binding to the immobilized EVL protein are presented.

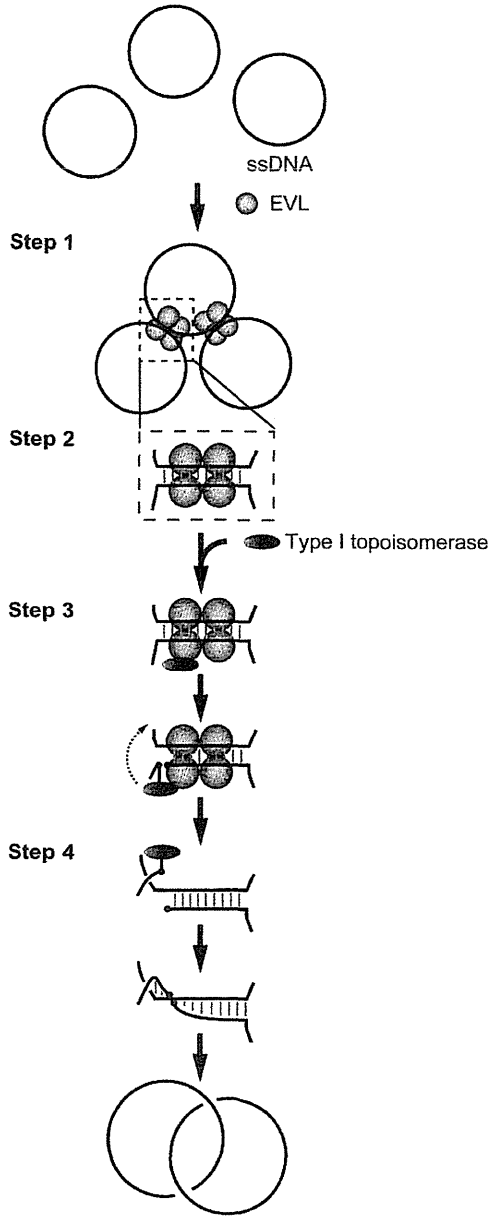

Figure 7. Model for the ssDNA-catenating reaction by EVL and a type I topoisomerase.

region, which may be evolutionarily conserved with TOPO IIIα, may enhance the ssDNA-catenating reaction *in vitro*.

DISCUSSION

In the present study, we found that human EVL and a type I topoisomerase promote the catenation of ssDNA molecules. It has been reported that RecA, a bacterial recombinase, promotes hemicatenation between ssDNA and dsDNA in the presence of Topo I (8); however, no report for the ssDNA-catenating reaction has been published thus far. We also confirmed that both prokaryotic and eukaryotic type I topoisomerases are functional for the ssDNA catenation with EVL.

Type I topoisomerase promotes cutting and rejoining reactions on a strand within dsDNA. In the present study, we showed that the annealing activity of EVL plays an essential role in the ssDNA-catenating reaction with a type I topoisomerase. Therefore, we have proposed an annealing-mediated model for the ssDNA-catenating reaction (Figure 7). In this model, EVL first binds to ssDNA and forms large complexes, each containing multiple ssDNA molecules (Step 1). Since human EVL contains a tetramerization domain at its C-terminus (21), the formation of multiple ssDNA complexes may be mediated through its tetramerization activity. The short complementary sequences of the ssDNA may be annealed within the EVL-multiple ssDNA complexes (Step 2). A type I topoisomerase, which may be recruited on the ssDNA annealed sites through binding to EVL, then cuts an ssDNA strand within the annealed region (Step 3). This nicked site rotates and rejoins (Step 4).

The functional significance of the ssDNA catenation by EVL and topoisomerases remains to be elucidated; however, it may be involved in homologous recombination because EVL directly interacts with the eukaryotic RecA homologs, RAD51 and RAD51B (2). Our previous analyses suggested that EVL may function as a RAD51 mediator, which stimulates the RAD51-mediated homologous-pairing and strand-exchange reactions (2,7). The ssDNA-catenating activity, comprising the ssDNA cutting and rejoining reactions, may be utilized to process the DNA intermediates formed by the homologous-pairing and strand-exchange reactions by RAD51. In the homologous-recombination process, it has been proposed that a DNA intermediate containing a D-loop, in which the ssDNA has invaded a homologous region of the intact dsDNA, is first formed by the RAD51-mediated homologous pairing. After this homologous-pairing step, the invading strand primes repair synthesis of the DNA strands, and the D-loop structure is converted to a four-way junction, the Holliday-junction intermediate, which moves along the DNA to expand the newly paired heteroduplex region. The ssDNA cutting and rejoining activities of EVL and topoisomerase may be involved in the conversion process from the D-loop to Holliday junction intermediates.

Alternatively, the ssDNA cutting and rejoining activities may function in the resolution of the Holliday junction. The Holliday-junction intermediate must be resolved into two parental DNA molecules by the ssDNA-nicking activity in the late stage of the homologous-recombination pathway. Interestingly, human TOPO IIIα, which was found to promote the ssDNA-catenating reaction with EVL, is reportedly involved in Holliday junction dissolution (13–16). In addition, EVL is known to bind RAD51B, which preferentially binds to the Holliday junction (2,22). Therefore, EVL may also be involved in the late stage of the HRR pathway, together with TOPO IIIα. Further analyses are required to clarify these issues.

ACKNOWLEDGEMENT

H. K. is a research fellow in the Waseda Research Institute for Science and Engineering.

FUNDING

Grants-in-Aid from the Ministry of Education, Culture, Sports, Science and Technology (MEXT), and the Japanese Society for the Promotion of Science (JSPS) of Japan. Funding for open access charge: Waseda University.

Conflict of interest statement. None declared.

REFERENCES

1. Kwiatkowski,A.V., Gertler,F.B. and Loureiro,J.J. (2003) Function and regulation of Ena/VASP proteins. *Trends Cell. Biol.*, **13**, 386–392.
2. Takaku,M., Machida,S., Hosoya,N., Nakayama,S., Takizawa,Y., Sakane,I., Shibata,T., Miyagawa,K. and Kurumizaka,H. (2009) Recombination activator function of the novel RAD51- and RAD51B-binding protein, human EVL. *J. Biol. Chem.*, **284**, 14326–14336.
3. Symington,L.S. (2002) Role of RAD52 epistasis group genes in homologous recombination and double-strand break repair. *Microbiol. Mol. Biol. Rev.*, **66**, 630–670.
4. West,S.C. (2003) Molecular views of recombination proteins and their control. *Nat. Rev. Mol. Cell. Biol.*, **4**, 435–445.
5. Sung,P., Krejci,L., Van Komen,S. and Sehorn,M.G. (2003) Rad51 recombinase and recombination mediators. *J. Biol. Chem.*, **278**, 42729–42732.
6. San Filippo,J., Sung,P. and Klein,H. (2008) Mechanism of eukaryotic homologous recombination. *Annu. Rev. Biochem.*, **77**, 229–257.
7. Takaku,M., Machida,S., Nakayama,S., Takahashi,D. and Kurumizaka,H. (2009) Biochemical analysis of the human EVL domains in homologous recombination. *FEBS J.*, **276**, 5841–5848.
8. Cunningham,R.P., Wu,A.M., Shibata,T., DasGupta,C. and Radding,C.M. (1981) Homologous pairing and topological linkage of DNA molecules by combined action of *E. coli* RecA protein and topoisomerase I. *Cell*, **24**, 213–223.
9. Harmon,F.G., DiGate,R.J. and Kowalczykowski,S.C. (1999) RecQ helicase and topoisomerase III comprise a novel DNA strand passage function: a conserved mechanism for control of DNA recombination. *Mol. Cell*, **3**, 611–620.
10. Harmon,F.G., Brockman,J.P. and Kowalczykowski,S.C. (2003) RecQ helicase stimulates both DNA catenation and changes in DNA topology by topoisomerase III. *J. Biol. Chem.*, **278**, 42668–42678.
11. Wu,L., Davies,S.L., North,P.S., Goulaouic,H., Riou,J.F., Turley,H., Gatter,K.C. and Hickson,I.D. (2000) The Bloom's syndrome gene product interacts with topoisomerase III. *J. Biol. Chem.*, **275**, 9636–9644.
12. Cheok,C.F., Bachrati,C.Z., Chan,K.L., Ralf,C., Wu,L. and Hickson,I.D. (2005) Roles of the Bloom's syndrome helicase in the maintenance of genome stability. *Biochem. Soc. Trans.*, **33**, 1456–1459.
13. Wu,L. and Hickson,I.D. (2003) The Bloom's syndrome helicase suppresses crossing over during homologous recombination. *Nature*, **426**, 870–874.
14. Wu,L., Bachrati,C.Z., Ou,J., Xu,C., Yin,J., Chang,M., Wang,W., Li,L., Brown,G.W. and Hickson,I.D. (2006) BLAP75/RMI1 promotes the BLM-dependent dissolution of homologous recombination intermediates. *Proc. Natl Acad. Sci. USA*, **103**, 4068–4073.
15. Raynard,S., Bussen,W. and Sung,P. (2006) A double Holliday junction dissolvasome comprising BLM, topoisomerase IIIalpha, and BLAP75. *J. Biol. Chem.*, **281**, 13861–13864.
16. Bussen,W., Raynard,S., Busygina,V., Singh,A.K. and Sung,P. (2007) Holliday junction processing activity of the BLM-Topo IIIalpha-BLAP75 complex. *J. Biol. Chem.*, **282**, 31484–31492.
17. Raynard,S., Zhao,W., Bussen,W., Lu,L., Ding,Y.Y., Busygina,V., Meetei,A.R. and Sung,P. (2008) Functional role of BLAP75 in BLM-topoisomerase IIIalpha-dependent holliday junction processing. *J. Biol. Chem.*, **283**, 15701–15708.
18. Singh,T.R., Ali,A.M., Busygina,V., Raynard,S., Fan,Q., Du,C.H., Andreassen,P.R., Sung,P. and Meetei,A.R. (2008) BLAP18/RMI2, a novel OB-fold-containing protein, is an essential component of the Bloom helicase-double Holliday junction dissolvasome. *Genes Dev.*, **22**, 2856–2868.
19. Henricksen,L.A., Umbricht,C.B. and Wold,M.S. (1994) Recombinant replication protein A: expression, complex formation, and functional characterization. *J. Biol. Chem.*, **269**, 11121–11132.
20. Bradford,M.M. (1976) A rapid and sensitive method for the quantitation of microgram quantities of protein utilizing the principle of protein-dye binding. *Anal. Biochem.*, **72**, 248–254.
21. Bachmann,C., Fischer,L., Walter,U. and Reinhard,M. (1999) The EVH2 domain of the vasodilator-stimulated phosphoprotein mediates tetramerization, F-actin binding, and actin bundle formation. *J. Biol. Chem.*, **274**, 23549–23557.
22. Yokoyama,H., Kurumizaka,H., Ikawa,S., Yokoyama,S. and Shibata,T. (2003) Holliday junction binding activity of the human Rad51B protein. *J. Biol. Chem.*, **278**, 2767–2772.

THE JOURNAL OF BIOLOGICAL CHEMISTRY VOL. 285, NO. 38, pp. 29662–29670, September 17, 2010

Ataxia Telangiectasia Mutated (ATM)-mediated DNA Damage Response in Oxidative Stress-induced Vascular Endothelial Cell Senescence*[S]

Received for publication, March 24, 2010, and in revised form, July 15, 2010 Published, JBC Papers in Press, July 16, 2010, DOI 10.1074/jbc.M110.125138

Hong Zhan[‡1], **Toru Suzuki**[‡§1,2], **Kenichi Aizawa**[‡§1], **Kiyoshi Miyagawa**[¶], **and Ryozo Nagai**[‡3]

From the Departments of [‡]*Cardiovascular Medicine,* [§]*Ubiquitous Preventive Medicine, and* [¶]*Radiation Biology, Graduate School of Medicine, The University of Tokyo, 7-3-1 Hongo, Bunkyo, Tokyo 113-8655, Japan*

Oxidative stress regulates dysfunction and senescence of vascular endothelial cells. The DNA damage response and its main signaling pathway involving ataxia telangiectasia mutated (ATM) have been implicated in playing a central role in mediating the actions of oxidative stress; however, the role of the ATM signaling pathway in vascular pathogenesis has largely remained unclear. Here, we identify ATM to regulate oxidative stress-induced endothelial cell dysfunction and premature senescence. Oxidative stress induced senescence in endothelial cells through activation/phosphorylation of ATM by way of an Akt/p53/p21-mediated pathway. These actions were abrogated in cells in which ATM was knocked down by RNA interference or inhibited by specific inhibitory compounds. Furthermore, the *in vivo* significance of this regulatory pathway was confirmed using ATM knock-out mice in which induction of senescent endothelial cells in the aorta in a diabetic mouse model of endothelial dysfunction and senescence was attenuated in contrast to pathological changes seen in wild-type mice. Collectively, our results show that ATM through an ATM/Akt/p53/p21-dependent signaling pathway mediates an instructive role in oxidative stress-induced endothelial dysfunction and premature senescence.

The DNA damage response is activated in response to stimuli ranging from oxidative stress, oncogenic stress to ionizing radiation to determine which cells remain viable after cytopathogenic insult. Recent reports suggest that the DNA damage response in addition to its classical role in regulating the cell cycle checkpoint in cancer to also play a major regulatory role in nononcogenic fields such as in aging/senescence (1–3). One field in which the DNA damage response has remained poorly addressed is the cardiovasculature.

Aging is known to be a major cardiovascular risk factor (4). Premature senescence in endothelial cells is induced by proatherogenic and proinflammatory factors such as hydrogen peroxide (H_2O_2), oxidized LDL or TNF-α by telomeric inactivation through an Akt-dependent mechanism (5, 6). Because regulation of aging/senescence of the vasculature, notably through the endothelial cell, contributes to mechanisms of arteriosclerosis and other age-related cardiovascular diseases (7), we questioned whether the DNA damage response might play a role in regulation of endothelial regulation of aging/senescence. For this, we focused on the role of ataxia telangiectasia mutated (ATM),[4] which is the central effector molecule in the DNA damage response pathway.

ATM belongs to the phosphoinositide 3-kinase (PI3-kinase)-related protein kinase (PIKK) family which has been identified as the product mutated or inactivated in ataxia telangiectasia (A-T) patients. The DNA damage response and its main signaling pathway involving ATM have been implicated in playing a central role in mediating the actions of oxidative stress (8–10). However, the role of the ATM signaling pathway in vascular pathogenesis has remained unclear. Further, pathogenic mechanisms of the vascular pathologies associated with mutated ATM (telangiectasia, premature coronary artery disease) remain obscure.

In the present study, we examined the effects of ATM-mediated oxidative stress-induced senescence in vascular pathologies through actions on endothelial cells. Our results show that ATM through an ATM/Akt/p53/p21-dependent signaling pathway mediates an instructive role in oxidative stress-induced endothelial dysfunction and premature senescence.

EXPERIMENTAL PROCEDURES

Cell Culture—Human umbilical vein endothelial cells (HUVECs) were purchased from Sanko Junyaku (Tokyo, Japan) and maintained with endothelial cell basal medium-2 containing EGM-2 supplement as purchased from Cambrex Bio Science (Rockland, MD) in humidified air with 5% CO_2 at 37 °C. All experiments were performed between passages 4 and 6.

Western Blot Analysis and Antibodies—HUVECs (3×10^5 cells/well) were treated with 100 μM H_2O_2 in the absence or presence of *N*-acetyl-L-cysteine (NAC) (Sigma-Aldrich), caffeine (Wako, Osaka, Japan), or KU-55933 (Calbiochem). Cells were washed with cold phosphate-buffered saline (PBS) and

* This work was supported by grants-in-aid for scientific research (T. S., K. A., and R. N.) from the Ministry of Education, Culture, Sports, Science, and Technology, Japan.

[S] The on-line version of this article (available at http://www.jbc.org) contains supplemental Experimental Procedures and Figs. 1–7.

[1] These authors contributed equally to this work.

[2] To whom correspondence may be addressed: Dept. of Cardiovascular Medicine, Graduate School of Medicine, The University of Tokyo, 7-3-1 Hongo, Bunkyo, Tokyo 113-8655, Japan. Tel.: 81-3-5800-9846; Fax: 81-3-5800-9847; E-mail: torusuzu-tky@umin.ac.jp.

[3] To whom correspondence may be addressed. Tel.: 81-3-5800-6526; Fax: 81-3-3815-2087; E-mail: nagai-tky@umin.ac.jp.

[4] The abbreviations used are: ATM, ataxia telangiectasia mutated; A-T, ataxia telangiectasia; BisTris, bis(2-hydroxyethyl)iminotris(hydroxymethyl)methane; DSB, DNA double-strand break; HUVEC, human umbilical vein endothelial cell; NAC, *N*-acetyl-L-cysteine; SA-β-gal, senescence-associated β-galactosidase; STZ, streptozotocin.

lysed with 2× NuPAGE LDS sample buffer (Invitrogen) supplemented with 1 mM sodium orthovanadate (Sigma-Aldrich) and 1 mM sodium fluoride (Wako). Lysates were then boiled for 10 min and centrifuged for 2 min at 4 °C. Equal amounts of protein were separated by NuPAGE 3–8% Tris acetate mini gel electrophoresis or NuPAGE 10% BisTris gel (Invitrogen) and then transferred onto a polyvinylidine difluoride (PVDF) membrane (Invitrogen). Membranes were blocked with 5% skim milk in PBS at room temperature for 1 h and then subsequently probed with primary antibodies at a predetermined optimal concentration for 2–4 h at room temperature or overnight at 4 °C. After rinsing with TBS containing 0.1% Triton X-100 (TBS-T), membranes were incubated with appropriate horseradish peroxidase-conjugated anti-rabbit (Cell Signaling Technology) or anti-mouse IgG (GE Healthcare) for 1 h at room temperature. After three washes with TBS-T, immunoblots were detected using the ECL Plus Western blotting Detection System (GE Healthcare) and exposed to x-ray film (Fuji medical x-ray film, Tokyo, Japan). Anti-phospho-ATM (Ser^{1981}) antibody was purchased from Millipore; anti-ATM (2C1) and anti-p53 (DO-1) antibodies were from Santa Cruz Biotechnology (Santa Cruz, CA); and anti-phospho-p53 (Ser^{15}), anti-phospho-Akt (Ser^{473}), and anti-Akt antibodies were from Cell Signaling Technology. Anti-GAPDH antibody (Life Technologies) was used as a loading control. Purified mouse anti-p21 antibody was obtained from BD Pharmingen. See also supplemental Experimental Procedures.

Immunofluorescence Microscopy—Cells were grown on coverslips at a density of 1×10^5 per slide. After treatment with 100 μM H_2O_2 for 1 h, cells were fixed in 3% paraformaldehyde in PBS for 10 min. Chamber slides were washed three times with PBS and then permeabilized with 0.25% Triton X-100 in PBS for 10 min. After washing twice with PBS and blocking for 5 min with 0.1% gelatin, slides were incubated with primary antibody (1:100) in 0.1% gelatin in PBS for 1 h in a humidified chamber at 37 °C. Cells were blocked three times with 0.1% gelatin, and then samples were incubated with secondary antibody using Alexa Fluor 488 green or Alexa Fluor 635 red (Life Technologies) in 0.1% gelatin in PBS for 1 h in a humidified chamber at 37 °C. Antibodies used for immunofluorescence were ATM-Ser^{1981}, ATM, p53-Ser^{15}, p53, p21, and 53BP1 (Cell Signaling Technology). Nuclei were stained with Hoechst 33258 and mounted with DakoCytomation Fluorescent Mounting Medium (Dako Japan, Kyoto, Japan) and then visualized with a Carl Zeiss LSM510 confocal microscope (Carl Zeiss, Jena, Germany).

Senescence-induced by Oxidative Stress and Senescence-associated β-Galactosidase (SA-β-gal) Staining—Methods for inducing premature senescence by H_2O_2 (Wako) have been described previously (11). Briefly, HUVECs (3×10^5 cells/well) were grown in 30-mm collagen-coated dishes to 80% confluence. Cells were pretreated for 3 days with vehicle, NAC (0.1, 2, and 10 mM), caffeine (0.1, 2, and 5 mM), or KU-55933 (0.5, 5, and 10 μM). After washing three times with endothelial cell basal medium-2 and treating for 1 h with 100 μM H_2O_2, cells were trypsinized, reseeded at a density of 5×10^4 in 30-mm dishes, and cultured with endothelial cell basal medium-2 containing compound for 10 days. Cells were then washed in PBS and fixed for 5 min at room temperature in 2% formaldehyde/0.2% glutaraldehyde, washed, and then incubated at 37 °C for 12 h (without CO_2) with fresh SA-β-gal stain solution which contained 1 mg/ml 5-bromo-4-chloro-3-indolyl-β-D-galactoside (X-Gal), 40 mM citric acid/sodium phosphate, pH 6.0, 5 mM potassium ferrocyanide, 5 mM potassium ferricyanide, 150 mM sodium chloride, and 2 mM magnesium chloride. Senescent cells were identified as blue-stained cells by phase contrast microscopy, and a total of 1,000 cells were counted in 20 random fields to determine the percentage of SA-β-gal-positive cells.

RNA Interference—Small interference RNA (siRNA) constructs were obtained as siGENOME SMARTpool reagent from Dharmacon. See also supplemental Experimental Procedures. A siRNA pool specific for ATM (siGENOME SMARTpool Human ATM, M-003201020005) and control siRNA (siGENOME nontargeting siRNA pool, D-0012061320) were used. HUVECs (3×10^5 cells/well) were grown to 80% confluence in 6-well culture dishes. Transient transfections of 10, 50, and 100 pmol of ATM siRNA or nontarget siRNA were performed by a liposome-mediated method using Lipofectamine 2000 according to the manufacturer's instructions (Invitrogen). The indicated amounts of siRNA and 5 μl of Lipofectamine 2000 were, respectively, diluted in 0.25 ml of Opti-MEM without serum. After incubation for 5 min, diluted siRNA and Lipofectamine 2000 were combined, and the mixture was incubated for 20 min at room temperature to allow the DNA·Lipofectamine 2000 complexes to form. 0.5 ml of complex was added to each well. After 5 h of transfection, the medium with complexes was removed, and endothelial cell basal medium-2 supplemented with EGM-2 was added. At 72 h following transient transfection, total RNA was extracted and submitted to reverse transcription-PCR (RT-PCR) experiments using oligonucleotide primers specific to ATM and 18 S rRNA. In ATM knock-down cells, the levels of total ATM, phospho-p53 (Ser^{15}), phospho-Akt (Ser^{473}), total Akt, or GAPDH proteins were analyzed by Western blotting, or SA-β-gal activity was measured.

RNA Extraction and Quantitative RT-PCR—Total RNA from HUVECs (3×10^5 cells/well) was extracted by the RNeasy Mini kit (Qiagen) according to the manufacturer's instructions. RNA concentration and purity were determined on a spectrophotometer (Ultrospec 3000; GE Healthcare) by calculating the ratio of optical density at 260 nm to 280 nm. One microgram of total RNA sample was used to generate first-strand complementary DNA by using powerscript reverse transcriptase (Clontech) according to the manufacturer's recommended procedures. PCR was then performed for ATM from the same complementary DNA samples using HotStarTaq (Qiagen), 10× PCR buffer, and 2.5 mM dNTP mix. The forward primer 5′-GATGTTGTTGTCCCTACTATGG-3′ and the reverse primer 5′-GCTACACTGCGCGTATAAGCC-3′ corresponded to human ATM. 18 S rRNA (Life Technologies) was used as an internal control. Amplification was initiated by 15 min of denaturation at 95 °C for 1 cycle followed by 30 cycles at 95 °C for 30 s, 57 °C for 30 s, and 72 °C for 40 s. After the last cycle of amplification, samples were incubated at 72 °C for 10 min in a GeneAmp™ PCR system (Applied Biosystems). PCR products, a 589-bp ATM fragment and a 350-bp 18 S fragment, were then visualized by UV

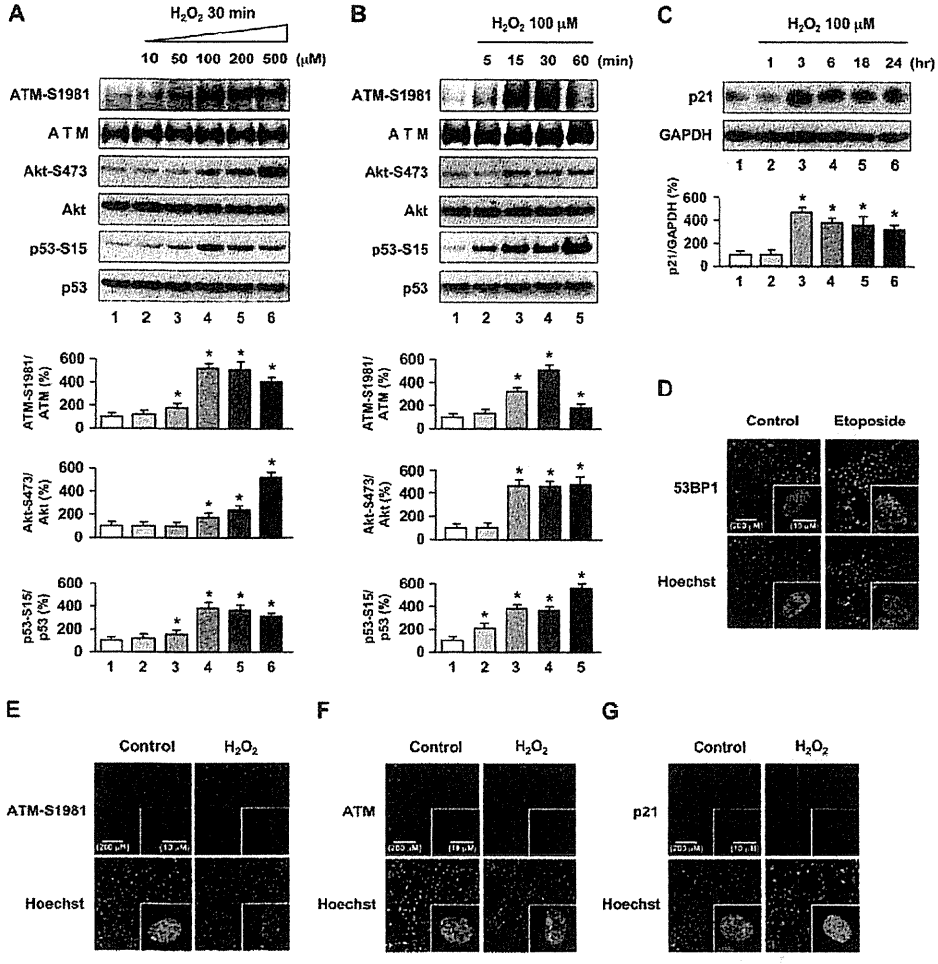

FIGURE 1. **Oxidative stress induces ATM-S1981, Akt-S473, p53-S15 phosphorylation and up-regulation of p21 expression in HUVECs.** *A*, cells were incubated with H_2O_2 for 30 min at the indicated concentrations. *B* and *C*, HUVECs were incubated in 100 μM H_2O_2 for the indicated times. Cells were lysed and subjected to Western blot analyses with the indicated antibodies. GAPDH was used as loading control. Values are mean ± S.E. (*error bars*) ($n = 3$). *, $p < 0.05$ *versus* cells incubated without H_2O_2 treatment. Representative blots are shown in the *upper panels* whereas corresponding quantitation is shown in the *lower panels*. *D–F*, immunofluorescence for 53BP1, phosphorylated ATM-S1981, and total ATM is shown. Cells were exposed to 10 μM etoposide or 100 μM H_2O_2 for 1 h and then immunostained for 53BP1 (*D*), ATM-S1981 (*E*) and total ATM (*F*). Cells incubated without etoposide or H_2O_2 were used as controls. *G*, cells were exposed to 100 μM H_2O_2 for 3 h and then immunostained for p21. Hoechst 33258 was used as nuclear stain (*blue*). Original magnification, ×200 and ×630. *Scale bars*, 200 μm and 10 μm, respectively. Treatment with etoposide and immunofluorescence for 53BP1 (labeled by green fluorescence) was used for a positive control. Expression of phosphorylated ATM-S1981) and p21 labeled by red fluorescence in HUVECs and foci formation was significantly increased after H_2O_2 treatment. Additional views of the photographs are shown in supplemental Fig. 1.

illumination after electrophoresis by 2% agarose gels containing 0.5 μg/ml ethidium bromide.

Animal Experiments—ATM knock-out mice (129S6/SvEvTac-*Atm*^{tm1Awb}/J) were obtained from Jackson Laboratories. All generations were from matings of heterozygous parents. The following sequence, as recommended by Jackson Laboratories, was used for genotyping: oIMR640, 5′-GCTGCCATACTTGATCAATG-3′; oIMR641, 5′-TCCGAATTTGCAGGAGTG-3′; oIMR0013, 5′-CTTGGGTGGAGAGGCTATTC-3; and oIMR0014, 5′-AGGTGAGATGACAGGAGATC-3′. Age-matched 10-week-old SPF male ATM wild-type ($^{+/+}$), heterozygote ($^{+/-}$), and homozygote ($^{-/-}$) mice ($n = 6$, respectively, weighing ~15–25 g) were used. Hyperglycemia was induced by a single intraperitoneal injection of streptozotocin (STZ) (180 mg/kg; Sigma-Aldrich). Tail blood glucose was assayed 3 days after injection using glucose test strips (Roche Applied Science). All diabetic animals had blood glucose values >300 mg/dl. Mice were housed under constant temperature (23 ± 1 °C) with a 12-h light and 12-h dark cycle for 10 days with free access to water and chow and were killed by cervical dislocation. The aorta was removed after systemic perfusion with PBS for histological examination. The aorta was fixed for 30 min at room temperature in 2% formaldehyde/0.2% glutaraldehyde, washed, incubated at 37 °C for 24 h (without CO_2) with fresh SA-β-gal stain solution, and then embedded in OTC compound before freezing in liquid nitrogen. The samples were stored at −80 °C until sample slides were prepared. The proportion of SA-β-gal-positive cells were analyzed by Scion Image software. Serial cross-sections (10 μm) were obtained from each sample and stained with kernechtrot staining solution (Muto, Tokyo, Japan) or prepared for immunohistochemistry. All experimental protocols complied with the guidelines for animal experiments of the University of Tokyo.

Tissue Protein Extraction—Thoracic aorta of ATM knock-out mice (ATM$^{+/+}$, ATM$^{+/-}$, ATM$^{-/-}$ mice) were dissected out of their thoracic aortas and snap frozen in liquid nitrogen. After thawing on ice, the thoracic aortas were homogenized mechanically at 25 Hz for 25 s five times on ice in 150 μl of RIPA buffer (0.1% SDS, 0.5% Nonidet P-40, 0.1% sodium deoxycholate, 150 mM NaCl, 50 mM Tris-HCl, pH 7.9, and 1× EDTA-free complete proteinase inhibitor (Roche Applied Science)). Samples were lysed gently on ice for 30–60 min, and cellular debris was removed by centrifugation. Protein was then quantified using the BCA protein assay kit (Thermo). A 30-μg aliquot of total protein was analyzed for ATM protein by Western blot analysis. Anti-GAPDH antibody was used as a loading control.

Immunohistochemistry—Immunostaining was performed using the Envision kit (Dako Japan). Frozen sections, 10 μm thick, were fixed in acetone at 4 °C, washed in TBS, and then blocked by 0.03% hydrogen peroxidase in methanol. After blocking nonspecific antibody-binding sites, the sections were incubated for 1 h with antibodies against von Willebrand factor (1:1,000; Abcam), p21 and p16 (Santa Cruz Biotechnology) as the primary antibody and then for 1 h with the peroxidase-

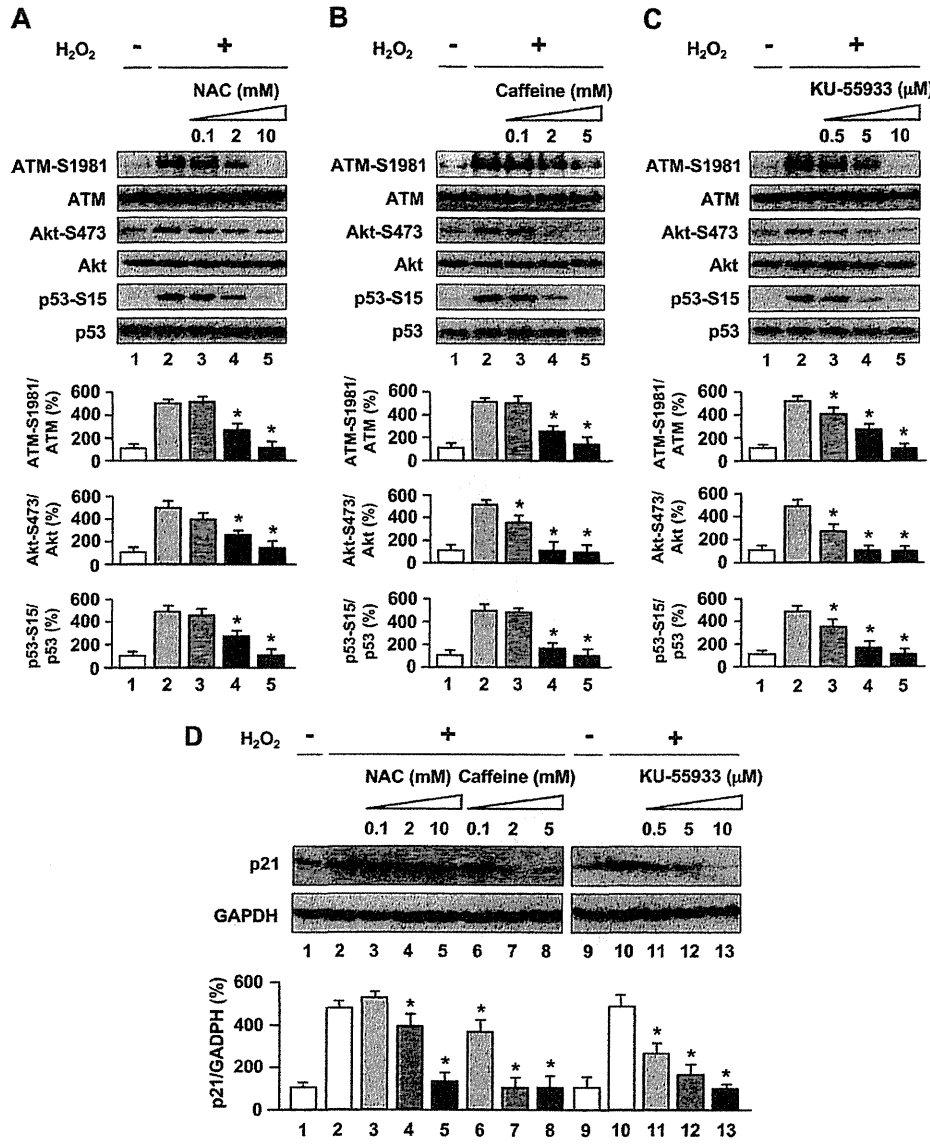

FIGURE 2. **Oxidative stress-induced Akt and p53 phosphorylation and up-regulation of p21 expression are dependent on ATM kinase.** *A–C*, antioxidant and ATM inhibitors blocked phosphorylation of ATM-S1981, Akt-S473, and p53-S15 as stimulated by H_2O_2 exposure. Cells were treated with 100 μM H_2O_2 for 30 min in the absence or presence of NAC (*A*) or caffeine (*B*), or KU-55933 (*C*), and whole cell lysates were subjected to Western blot analyses using the indicated antibodies. *D*, antioxidant and ATM inhibitors down-regulated p21 induction as stimulated by H_2O_2 exposure. Cells were pretreated with NAC, caffeine, or KU-55933 and then 100 μM H_2O_2 for 3 h. Whole cell lysates were subjected to Western blot analyses using p21 antibody. GAPDH was used as loading control. Values are mean ± S.E. (*error bars*) ($n = 3$). *, $p < 0.05$ *versus* cells incubated with H_2O_2. Representative blots are shown in the *upper panels* whereas corresponding quantitation is shown in the *lower panels*.

labeled polymer. Finally, sections were incubated with diaminobenzidine tetrahydrochloride (Dako Japan), and the nuclei were counterstained with hematoxylin.

Statistical Analysis—All values are expressed as mean ± S.E. Differences between two groups were analyzed using the two-tailed Student's *t* test. Threshold of significance was taken as $p < 0.05$.

RESULTS

ATM Is Activated by Oxidative Stress in Vascular Endothelial Cells—To investigate the involvement of ATM in mediating oxidative stress in the vasculature, we first examined the activation and expression of ATM in cultured HUVECs treated with H_2O_2 as an inducing agent of oxidative stress. HUVECs exposed to H_2O_2 showed increased ATM phosphorylation at Ser^{1981} (ATM-S1981) (Fig. 1, *A* and *B*), which releases it from an inhibitory homodimer structure leading to its activation and recruitment to sites of DNA double-strand breaks (DSBs) (12–14). We next investigated factors involved in the ATM signaling pathway. Because ATM mediates activation of Akt in response to insulin or ionizing radiation which then in turn results in radiosensitivity or resistance to insulin in cell lines derived from A-T patients and ATM knock-out mice (15), we first investigated the activation of Akt in response to oxidative stress. Akt phosphorylation at Ser^{473} (Akt-S473) was increased in H_2O_2-treated HUVECs (Fig. 1, *A* and *B*). We then investigated involvement of p53, a downstream signaling molecule of ATM (10) and Akt (6), which showed phosphorylation at Ser^{15} (p53-S15) after exposure to H_2O_2 (Fig. 1, *A* and *B*). Furthermore, p21, a downstream target of p53, was increased in H_2O_2-treated HUVECs (Fig. 1*C*). Our results indicate that oxidative stress phosphorylates ATM and its involved genes, Akt and p53, with subsequent up-regulation of p21 expression. Thus, the phosphorylation of ATM, Akt, and p53 and up-regulation of p21 expression mediate actions of oxidative stress in endothelial cells.

Although ATM is predominantly present in the nucleus, a variable amount (<10%) has been reported in the cytoplasm, especially in neuronal cells. The major known role of nuclear ATM is to participate in the response to DSBs for DNA repair and cell cycle checkpoint activation (16). In response to agents that induce DSBs, ATM has been found to relocalize to the sites of breaks and in doing so forms large nuclear foci (17). To determine whether oxidative stress-induced ATM forms foci, immunofluorescence analyses for phospho-ATM (Ser^{1981}), total ATM, and p21 were performed. Increased fluorescence and foci formation were seen in response to H_2O_2 for phosphorylated ATM (Fig. 1*E* and supplemental Fig. 1*B*) and increased p21 (Fig. 1*G* and supplemental Fig. 1*D*) under conditions in which 53BP1 formed nuclear foci in response to etoposide as reported

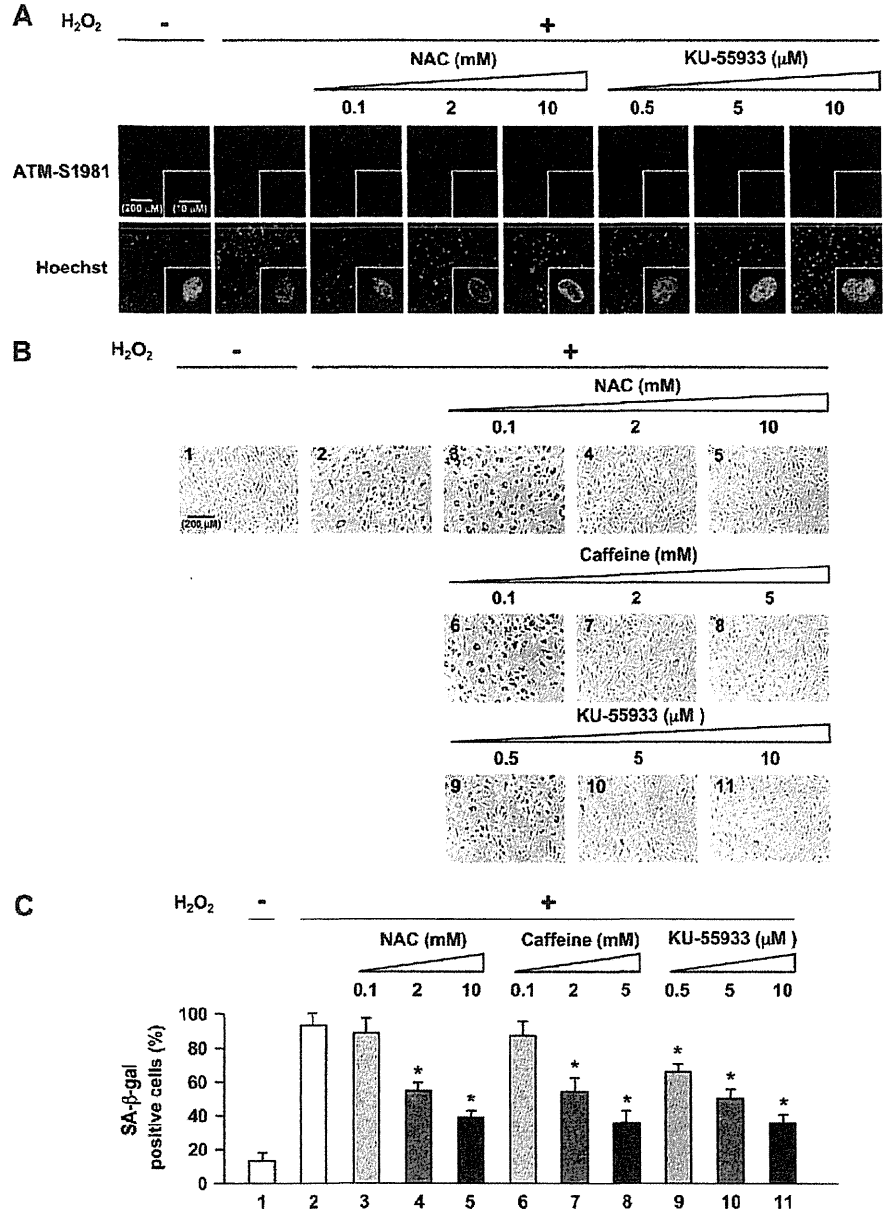

FIGURE 3. **Oxidative stress-induced endothelial cell senescence involves activation of ATM kinase.** *A*, immunofluorescence analysis of the effects of antioxidant (NAC) and ATM inhibitor (KU-55933) on phosphorylated ATM. Cells were treated with NAC or KU-55933 followed by 100 μM H_2O_2 for 1 h and then immunostained for phosphorylated ATM-S1981. Hoechst 33258 was used as nuclear stain (*blue*). Original magnification, ×200 and ×630. Higher magnification of the representative cells in *A* is shown in supplemental Fig. 2. *Scale bar*, 200 μm and 10 μm, respectively. NAC or KU-55933 greatly reduced phosphorylated ATM nuclear fluorescence and foci formation. *B*, effects of NAC, caffeine, or KU-55933 on premature senescent phenotype induced by H_2O_2 as shown by SA-β-gal staining. *C*, quantification of percentage of SA-β-gal-positive cells in *B*. Values are mean ± S.E. (*error bars*) ($n = 3$). *, $p < 0.05$ *versus* cells incubated with H_2O_2. Original magnification, ×100. *Scale bar*, 200 μm. Pretreatment with NAC, caffeine, or KU-55933 resulted in significant reduction of senescent (SA-β-gal-positive) cells compared with those exposed to H_2O_2 alone.

(Fig. 1*D* and supplemental Fig. 1*A*) (18). Total ATM, in contrast, remained diffusely localized throughout the nucleus, and foci formation was not observed in H_2O_2-treated HUVECs (Fig. 1*F* and supplemental Fig. 1*C*). Activated (phosphorylated) ATM localized to foci, which suggests that it might be recruited to sites of DNA damage caused by oxidative stress (17, 18). However, the authors note that the antibody used (ATM-S1981) is known to also recognize a nonspecific protein, which makes conclusions based on experiments using this antibody inconclusive. We further investigated expression of 53BP1 and γ-H2AX as markers of DSB formation in response to H_2O_2 by immunostaining. In the H_2O_2-treated cells, both 53BP1 and γ-H2AX formed nuclear foci (supplemental Fig. 3), which further supports that ATM is activated in response to DSB formation induced by H_2O_2.

Activation of the ATM-dependent DNA Damage Signaling Pathway Contributes to Endothelial Cell Senescence—To better confirm actions of activation of ATM by oxidative stress in endothelial cells, effects of inhibitors of oxidative stress and of ATM were tested. HUVECs were pretreated with NAC, an antioxidant and glutathione precursor that alters the redox state of cells (19), to assess whether ATM phosphorylation was caused by H_2O_2-induced redox imbalance. Western blot analysis showed that pretreatment of endothelial cells with NAC blocked the stimulatory effects of H_2O_2 on the expression of ATM-S1981, Akt-S473, p53-S15 (*lanes 3–5* in Fig. 2*A*) and p21 (*lanes 3–5* in Fig. 2*D*). These results suggest a direct role of H_2O_2 in ATM phosphorylation and activation of involved genes. We further employed two inhibitors, caffeine and KU-55933, to inhibit ATM kinase activity to examine whether Akt and p53 activation as well as p21 up-regulation induced by H_2O_2 is dependent on the ATM protein kinase. Caffeine is known to disrupt ATM-dependent responses likely through direct inhibition of ATM kinase activity (20), and KU-55933 is a specific and potent inhibitor of ATM kinase (21). Both inhibitors inhibited H_2O_2-induced ATM (Ser^{1981}), Akt (Ser^{473}), and p53 (Ser^{15}) phosphorylation (*lanes 3–5* in Fig. 2, *B* and *C*), in addition to p21 induction (*lanes 6–8* and *lanes 11–13* in Fig. 2*D*). Thus, ATM kinase played a major role in transducing H_2O_2-induced DNA damage signaling in HUVECs. Because an Akt/p53/p21-dependent pathway has been reported in endothelial cells (6), ATM thus likely regulates the cellular response to oxidative stress via phosphorylation of Akt and p53 then induction of p21 in sequence. Furthermore, NAC or KU-55933 also

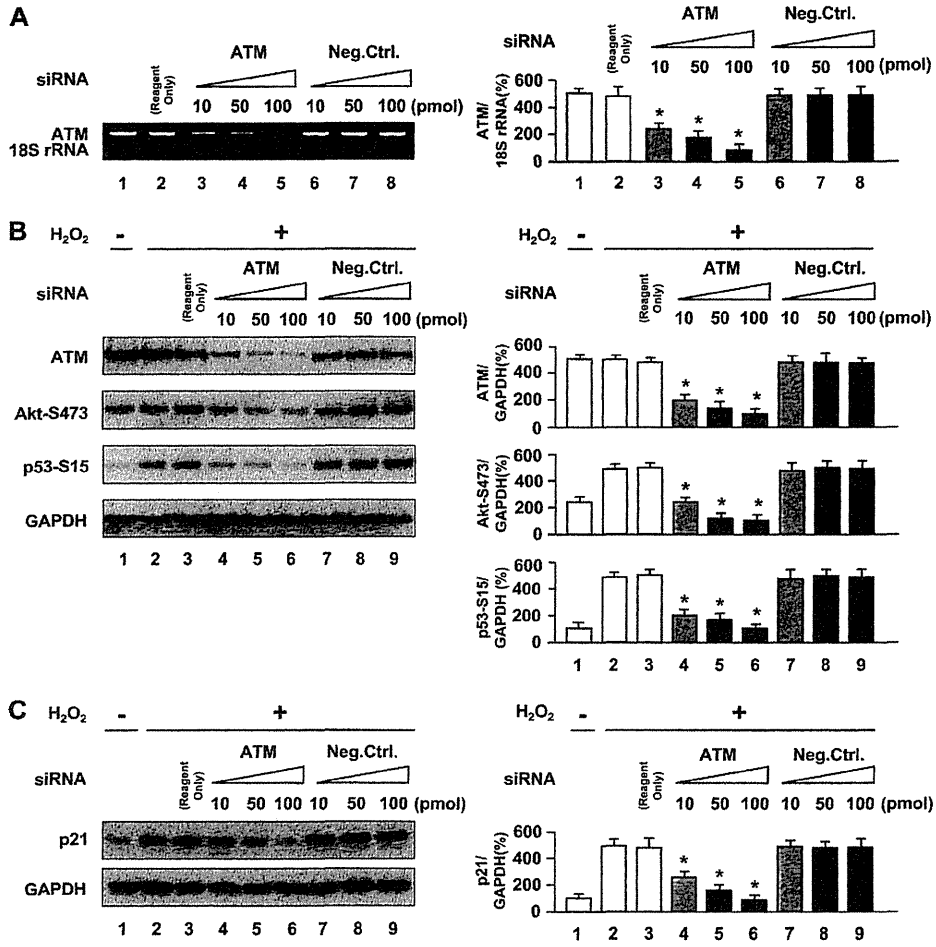

FIGURE 4. **Knockdown of ATM by ATM siRNA inhibits oxidative stress-induced activation of Akt and p53 and induction of p21 expression.** *A*, effect of siRNA against ATM on expression of ATM as analyzed by RT-PCR. *B* and *C*, Western blot analysis of the effects of siRNA against ATM on expression of total ATM, Akt phosphorylation (Ser^{473}), p53 phosphorylation (Ser^{15}), and p21 induction. Cells were transfected with siRNA against ATM for 72 h followed by incubation with 100 μM H_2O_2 for 30 min in *B* or 3 h in *C*. GAPDH was used as loading control. Values are mean ± S.E. (*error bars*) ($n = 3$). *, $p < 0.05$ *versus* cells transfected with the same concentration of negative control siRNA. Representative blots are shown in the *left panels* whereas corresponding quantitations are shown in the *right panels*. *Reagent Only*, cells transfected with Lipofectamine 2000 alone.

greatly reduced phosphorylated ATM nuclear fluorescence and foci formation (Fig. 3*A*). Collectively, H_2O_2 induced DNA damage and stimulated autophosphorylation of ATM in addition to formation of discrete nuclear foci together with subsequent induction of phosphorylation of Akt, p53, and up-regulation of p21 expression in an ATM-dependent manner.

Because the DNA damage response pathway triggers senescence (22) and because p53 and p21 were described to be major players in the induction of senescence (23, 24), we next addressed the functional effects of activation of the ATM/Akt/p53/p21 pathway on endothelial cells, namely in the form of induction of senescence which is a consequence of endothelial dysfunction. We induced premature endothelial senescence by addition of H_2O_2 to 100 μM as shown by SA-β-gal assay, a recognized surrogate index of senescent cells (25). We found that percentage of HUVECs positive for SA-β-gal was markedly increased in cells treated with H_2O_2, compared with cells incubated without H_2O_2 treatment (*panel 2* in Fig. 3*B* and *lane 2* in Fig. 3*C*). Furthermore, pretreatment with NAC, caffeine, or KU-55933 resulted in significant reduction of senescent (SA-β-gal-positive) cells compared with those exposed to H_2O_2 alone (Fig. 3, *B* and *C*). Thus, activation of ATM by H_2O_2 promotes endothelial cell senescence and contributes to vascular pathogenesis.

Abrogation of ATM Blocks Effects of Oxidative Stress on Endothelial Cells—We further examined the requirement of ATM expression in H_2O_2-induced premature senescence by abrogating ATM in cells using RNA interference. Knockdown of ATM in HUVECs by siRNA reduced ATM mRNA and protein levels (Fig. 4, *A* and *B*). Cells transfected with ATM siRNA showed reduced ATM expression with inhibition of Akt and p53 phosphorylation (*lanes 4–6* in Fig. 4*B*) in addition to down-regulation of p21 expression (*lanes 4–6* in Fig. 4*C*). As expected, ATM nuclear fluorescence was also markedly decreased in cells with ATM knocked down (Fig. 5*A*). Furthermore, knockdown of ATM by siRNA suppressed increase in SA-β-gal-positive cells induced by H_2O_2 (*panels 5* and *6* in Fig. 5*B* and *lanes 5* and *6* in Fig. 5*C*), which were comparable with the changes seen when HUVECs were treated with antioxidant or ATM inhibitor. Moreover, down-regulation of Akt, p53, or p21 by siRNA also suppressed an increase in SA-β-gal-positive cells induced by H_2O_2 (supplemental Figs. 4 and 5). Thus, RNA interference experiments further confirmed that ATM and its downstream molecules, Akt, p53, and p21, mediate actions of oxidative stress on endothelial cells to induce senescence.

Abrogation of Senescent Phenotype in Aorta of ATM Knock-out Mice—To test whether ATM mediates vascular endothelial cell senescence *in vivo*, we administered STZ to ATM knock-out mice and wild-type littermates to induce hyperglycemia-induced endothelial dysfunction because vascular endothelial cell senescence has been previously documented to be induced in STZ-diabetic mice (26). Western blot analysis for ATM protein levels in the thoracic aortas of heterozygous knock-out mice showed marked reductions to levels almost comparable with those of homozygote knock-out mice in contrast to robust levels as seen in wild-type mice (Fig. 6*B* and supplemental Fig. 7*A*) although the mechanisms of reduced protein levels in heterozygous knock-out mice are unclear. STZ-treated mice showed an elevation in blood glucose levels compared with STZ-untreated mice (*lanes 2, 4,* and *6* in Fig. 6*C*). SA-β-

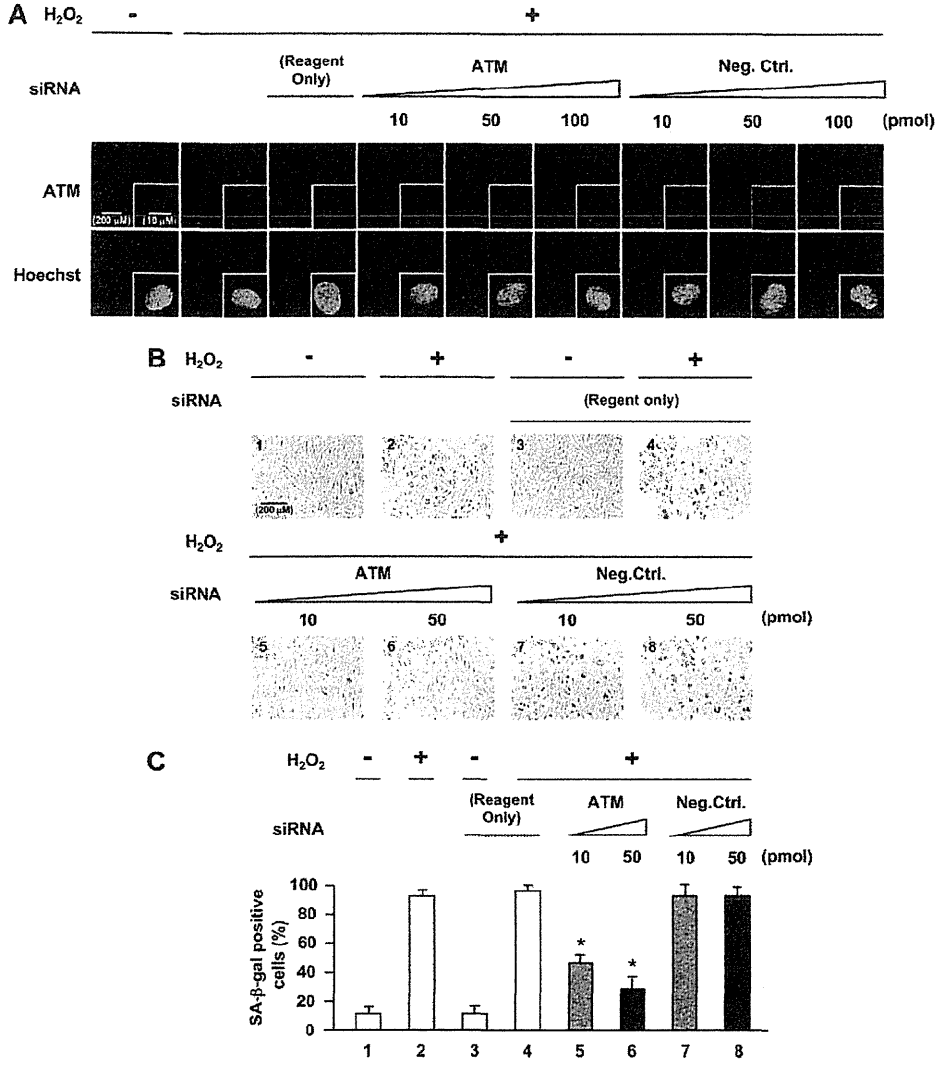

FIGURE 5. **Effects of abrogation of ATM expression by siRNA against ATM in oxidative stress-induced endothelial senescence.** *A*, immunofluorescence analysis of the effect of siRNA against ATM on total ATM. Transfected cells were immunostained for total ATM. Hoechst 33258 was used as nuclear stain (*blue*). Original magnification, ×200 and ×630. *Scale bar*, 200 μm and 10 μm, respectively. ATM nuclear fluorescence was greatly decreased in ATM knock-down cells. *B*, staining of SA-β-gal activity in ATM knock-down cells. *C*, quantification of percentage of SA-β-gal-positive cells in ATM knock-down cells. Values are mean ± S.E. (*error bars*) ($n = 3$). *, $p < 0.05$ *versus* cells transfected with the same concentration of negative control siRNA (*lane 7* or *lane 8*, respectively) ($n = 3$ each). Original magnification, ×100. *Scale bar*, 200 μm. *Reagent Only*, cells transfected with Lipofectamine 2000 alone. Knockdown of ATM by siRNA suppressed the increase in SA-β-gal-positive cells induced by H_2O_2.

gal activity was observed in the thoracic aortas of STZ-diabetic wild-type mice but not in STZ-diabetic ATM knock-out mice (Fig. 6, *D* and *E*). Cross-sections of thoracic aortas stained with SA-β-gal showed that positive areas were mostly localized to the luminal surface (Fig. 6*F*) which also stained positive for von Willebrand factor, indicating localization to vascular endothelial cells and not the extracellular matrix compared with normal rabbit IgG antibody (Fig. 6*G* and supplemental Fig. 6*A*). p21 and p16 are cyclin-dependent kinase inhibitor genes that are used as senescence markers. SA-β-gal-positive areas of cross-sections of thoracic aortas stained positive for p21 and p16 (Fig. 6*H* and 6*I*) but not for normal mouse IgG antibody used as a negative control (supplemental Fig. 6*B*). These results indicate that ATM is important for the induction of endothelial cell senescence in aortas of STZ-diabetic mice, which is consistent with *in vitro* cellular experiments.

DISCUSSION

Oxidative stress caused by reactive oxygen species plays an important causal role in senescence and age-related vascular diseases, including atherosclerosis and diabetic vasculopathy (7, 27, 28). Despite the wealth of knowledge on the effects and actions of oxidative stress on endothelial cells, characterization of involved regulatory pathways allowing for targeted molecular intervention with therapeutic intent had remained elusive.

We showed that ATM is involved in oxidative stress-induced endothelial dysfunction and premature senescencethroughanAkt/p53/p21-dependent pathway. Cellular experiments using HUVECs showed that the ATM/Akt/p53/p21 pathway was involved in oxidative stress-induced cellular senescence *in vitro*. Experiments using antioxidant and specific ATM inhibitory compounds or siRNA against ATM inhibited oxidative stress-induced cellular senescence thus confirming involvement of ATM and its dependent pathway. Furthermore, ATM induced endothelial cellular senescence *in vivo* in the aorta of diabetic wild-type mice but not in ATM knock-out mice. STZ-diabetic $ATM^{+/-}$ mice exhibit reduction in SA-β-gal-positive cells to levels almost comparable with those seen in STZ-diabetic $ATM^{-/-}$ mice. Reduction of ATM protein expression in heterozygote knock-out mice may account for the difference seen in endothelial senescence between wild-type and heterozygous knock-out mice. Collectively, the findings presented here indicate the importance of ATM in the induction of endothelial cell senescence induced by oxidative stress and abrogation of ATM resulting in a dysregulated response to pathophysiological stress in cardiovascular endothelial cells.

We further showed that ATM lies upstream from the Akt/p53/p21 pathway and that oxidative stress as sensed through ATM possibly in response to oxidative DNA damage is the initiating "trigger" and plays an instructive role in activation of this signaling pathway. Previous studies also demonstrated that ATM is a major upstream activator of Akt through control of